Article

Current Biology

DNA Damage Follows Repair Factor Depletion and Portends Genome Variation in Cancer Cells after Pore Migration

Graphical Abstract

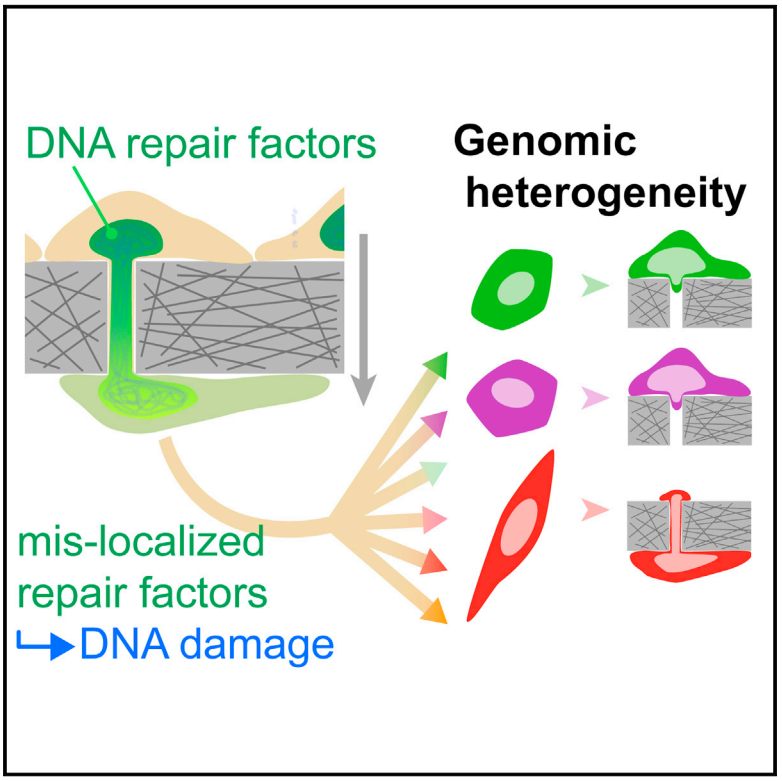

Authors

Jerome Irianto, Yuntao Xia, Charlotte R. Pfeifer, ..., Andrea J. Liu, Roger A. Greenberg, Dennis E. Discher

Correspondence

discher@seas.upenn.edu

In Brief

Irianto et al. demonstrate that cell migration through micron-size constrictions leads to transient DNA damage and cytoplasmic mis-localization of multiple DNA repair factors, with lasting genomic heterogeneity that translate to phenotypic changes. Migration-induced genomic instability can thus associate with heritable changes.

Highlights

- Constricted migration causes mis-localization of DNA repair proteins and DNA breaks
- Depletion of repair factors leads to DNA damage and chromosomal aberrations
- Migration of cancer clones through small pores causes lasting genomic heterogeneity
- Gene dosage effects in the transcriptome can perturb cell shape and motility

Irianto et al., 2017, Current Biology *27*, 210–223
January 23, 2017 © 2016 Elsevier Ltd.
http://dx.doi.org/10.1016/j.cub.2016.11.049

CellPress

CellPress

Current Biology
Article

DNA Damage Follows Repair Factor Depletion and Portends Genome Variation in Cancer Cells after Pore Migration

Jerome Irianto,[1,2] Yuntao Xia,[1,2] Charlotte R. Pfeifer,[1,2,3] Avathamsa Athirasala,[2] Jiazheng Ji,[1,2] Cory Alvey,[1,2] Manu Tewari,[1,2] Rachel R. Bennett,[1,3] Shane M. Harding,[1,4] Andrea J. Liu,[1,3] Roger A. Greenberg,[1,4] and Dennis E. Discher[1,2,3,5,*]

[1]Physical Sciences Oncology Center at Penn (PSOC@Penn)
[2]Molecular and Cell Biophysics Lab
[3]Graduate Group, Department of Physics and Astronomy
[4]Cancer Biology, Abramson Family Cancer Research Institute, Perelman School of Medicine
129 Towne Building, University of Pennsylvania, Philadelphia, PA 19104, USA
[5]Lead Contact
*Correspondence: discher@seas.upenn.edu
http://dx.doi.org/10.1016/j.cub.2016.11.049

SUMMARY

Migration through micron-size constrictions has been seen to rupture the nucleus, release nuclear-localized GFP, and cause localized accumulations of ectopic 53BP1—a DNA repair protein. Here, constricted migration of two human cancer cell types and primary mesenchymal stem cells (MSCs) increases DNA breaks throughout the nucleoplasm as assessed by endogenous damage markers and by electrophoretic "comet" measurements. Migration also causes multiple DNA repair proteins to segregate away from DNA, with cytoplasmic mis-localization sustained for many hours as is relevant to delayed repair. Partial knockdown of repair factors that also regulate chromosome copy numbers is seen to increase DNA breaks in U2OS osteosarcoma cells without affecting migration and with nucleoplasmic patterns of damage similar to constricted migration. Such depletion also causes aberrant levels of DNA. Migration-induced nuclear damage is nonetheless reversible for wild-type and sub-cloned U2OS cells, except for lasting genomic differences between stable clones as revealed by DNA arrays and sequencing. Gains and losses of hundreds of megabases in many chromosomes are typical of the changes and heterogeneity in bone cancer. Phenotypic differences that arise from constricted migration of U2OS clones are further illustrated by a clone with a highly elongated and stable MSC-like shape that depends on microtubule assembly downstream of the transcription factor GATA4. Such changes are consistent with reversion to a more stem-like state upstream of cancerous osteoblastic cells. Migration-induced genomic instability can thus associate with heritable changes.

INTRODUCTION

The nucleus has long been thought to limit a cell's ability to migrate through small, stiff pores in tissue matrix [1], but migration through constricting pores can also rupture the nuclear lamina [2]. Nuclear envelope rupture in migration through narrow channels causes GFP constructs with a nuclear localization signal (NLS) peptide to mis-localize into the cytoplasm for hours [3]. On the other hand, localized accumulations within the nucleus of GFP fusions of 53BP1—one of many DNA repair factors—has suggested increased DNA damage. Although such accumulations of GFP-53BP1 could be consistent with initial reports of DNA damage in constricted migration [2, 4], GFP itself has a nuclear localization tendency [5], and overexpression of nuclear proteins including 53BP1 can have important functional effects [6]. Moreover, in immortalized epithelial (RPE-1) cells, GFP-53BP1 only appeared to be enriched far from the leading-edge site of nuclear rupture and resolved within minutes [3], whereas in U2OS osteosarcoma cells, enrichment occurred only at the site of nuclear rupture and required hours to resolve [7]. Exposure of U2OS cells in 2D culture to DNA damage agents for 1 hr likewise causes damage that lasts for many hours [8], and that is prolonged upon depletion or mutation of chromatin binding [8] and DNA repair factors [9–11].

Here we focus first on spatiotemporal changes of endogenous DNA damage and repair factors in U2OS cells migrating through rigid micropores (of relevance to bone), and then we focus on lasting perturbations to the genome. U2OS cells are widely used for studies of genomic instability (e.g., [12]), in part because osteosarcoma tumors are multi-clonal, with changes of hundreds of megabases in multiple chromosomes [13, 14]. Chromosomal aberrations in osteosarcomas are also characteristic of DNA repair defects [15], motivating our scrutiny of endogenous repair factors. U2OS clones generated from single cells

CrossMark

ultimately provide key evidence of migration-induced genotype-phenotype changes.

RESULTS

Rupture, DNA Breaks, and Mis-localized Repair Factors after Constricted Migration

U2OS cells squeeze through transwell filters with 3-μm pores even with equal serum on both sides of the filters, and migration transforms the rounded nuclei (Figure 1A) into distorted, often elongated shapes with polar blebs on 90% of nuclei (Figure 1B). Lamin-A,C enrichment on blebs contrasts with lamin-B's near absence (Figures 1B and S1), similar to initial reports of lung carcinoma A549 cells [2]. Immunostaining for DNA damage marker γH2AX resolved 15–20 γH2AX foci in nuclei on transwell tops and in cells on glass, but γH2AX foci are greater (~60%) after constricted migration, independent of a serum gradient (Figures 1C–1E). As a nucleus exits a pore, γH2AX foci concentrate near the pore (Figure S1). For 8-μm pores, top (unmigrated) and bottom (migrated) cells show no difference in γH2AX foci numbers and nuclear blebs (Figures 1B, 1E, and S1).

Damage is also evident in mesenchymal stem cells (MSCs) and the A549 cells. Primary MSCs from human bone marrow are osteogenic but stop growing beyond approximately five passages [16] (especially post-migration), and they express abundant lamin-A that "freezes" in a highly elongated shape after pore migration [2]. However, migration increases nuclear blebs in MSCs (Figure S1) and A549s as noted [2], and both show more γH2AX foci post-migration (Figures 1F and S1).

Foci number with activated ATM (phosphorylated ATM that can phosphorylate H2AX, among other factors) is ~40% greater after U2OS cell migration through 3-μm, but not 8-μm, pores (Figure 1G). Electrophoresis-based "comet assays" of nuclei isolated post-migration relative to nuclei detached from transwell tops (Figure 1H) also showed more of a cathode-shifted centroid of DNA (by ~60% above a threshold) with a higher mean displacement. Etoposide treatment causes abundant DNA breaks as expected [17].

Micro-nuclei are satellite nuclei, often γH2AX positive, with roles in genome remodeling [18], but very few cells (2% top; 4% bottom) show micro-nuclei (Figure S1) compared to the 6- to 7-fold larger fractions of cells with significant DNA breaks in comet assays (Figure 1H). MDA-MB-231 cells show similar micro-nuclei counts [7]. Importantly, cultures of migrated U2OS cells reverse the nuclear blebs and γH2AX foci, indicating that such changes are transient (Figure 1I).

The DNA repair factors Ku80 and BRCA1 are diffusible [19, 20] and mis-localize to cytoplasm after constricted migration (Figures 2A, 2B, and S1). H2B-mCherry and GFP-NLS constructs also rupture from the fronts of nuclei in migration and re-localize within hours [3, 7, 21], whereas GFP-53BP1 seems to be delayed (Figure S1). Although overexpression of 53BP1 can rescue radiation-induced DNA damage in mouse embryo fibroblasts cultured from lamin-A knockout mice on rigid plastic [6], we find that overexpressed 53BP1 does not reproducibly rescue migration-induced DNA damage (Figure S1). However, repair involves multiple factors. Endogenous Ku80 and BRCA1 indeed exhibit low nuclear-to-cytoplasmic ratios after migration at population (Figure 2B) and single-cell (Figure 2C) levels. Low nuclear-to-cytoplasmic ratios of Ku80 and high γH2AX foci counts decay over hours (Figure 2C), consistent with timescales post-etoposide [8]. Such deficits in repair factors could have functional effects because mouse knockouts or heterozygous mutants for BRCA1, BRCA2, Ku80, ATM, and RPA1 can alter chromosome copy numbers [22–26]. All of these DNA repair factors are expressed in U2OS cells (Figure 3A), despite reported deficits (e.g., BRCA2 and p53 [15]), and variations between U2OS cultures pre- and post-migration are small. However, rupture-induced decreases in nuclear fractions of such diffusible factors can be expected to increase γH2AX foci throughout the nucleus, as seen here (Figure S1), rather than being enriched near the ruptured lamina [7].

Depletion of a Subset of Repair Factors Favors DNA Damage Accumulation, but Not Death

To begin to assess possible effects of partial loss of repair factors from U2OS nuclei, we partially knocked down BRCA1, BRCA2, Ku80, and RPA1 (Figures 3B and S2). DNA damage increases with knockdown of individual factors almost linearly (for RPA1) and almost additively for the combination (denoted si4) as shown by both γH2AX foci and comet assay (Figures 3C*i*, 3C*ii*, and S2). Foci are once again seen throughout the nucleus (Figure 3C*i*). Knockdown of BRCA2 notably increases γH2AX foci (Figure S2), despite BRCA2 being functionally low in U2OS cells [15]. ATM inhibitor (ATMi) did increase cell death in migration but did not affect comet assay results, probably because high dose ATMi affects stress pathways independent of DNA damage (Figure S2), and so we excluded ATM from si4. The si4 is intended to approximate nuclear depletion of multiple factors after constricted migration (Figures 2A, 2B, and S1), and the increased DNA damage is consistent with past studies of individual factors in other cells [28–31]. Control transfections with siCtrl/lipofectamine also increase DNA damage (by ~40% when averaged across all control assays) and might reflect cell stress in transfection [32]. Etoposide-induced γH2AX foci in U2OS cultures require many hours to resolve [8] and remain high with si4 (Figure 3C*iii*). Migration-induced mis-localization of multiple repair factors for many hours (Figures 2A–2C and S1) could thus delay repair so that damage accumulates (Figures 1C–1F)—as seen again with siCtrl cells (Figure 3D*i*, bottom versus top). Regardless, si4 knockdown cells on the bottom show the same high number of γH2AX foci as non-migrated cells on the top (Figure 3D*i*), and because cell death is also elevated with si4 (unlike control cells; Figure S2), the high number of foci might reflect maximum levels before γH2AX fills the nucleus and precipitates cell death.

A high level of DNA damage on the top with si4 (or etoposide) does not affect the fraction of cells that migrate through a pore (Figure 3D*ii* or Figure S2), and the fraction of cells that survive such migration can also be reduced pharmacologically without affecting DNA damage (Figure S2). This includes careful titrations with ATMi, an inihibitor of ATM kinase that exerts effects independent of DNA repair [33]. However, DNA staining analyses in interphase cells does show that si4 causes an increase in DNA levels per cell (Figures 3E and S2), and DNA content in some si4 cells also exhibits odd ploidy that can exceed 4N. Chromosome copy numbers could thus be imbalanced (as aneuploidy).

For high-resolution microscopy of chromosomes in a population of U2OS cells that were genomically homogeneous to start with, U2OS clones were generated by expansion of single

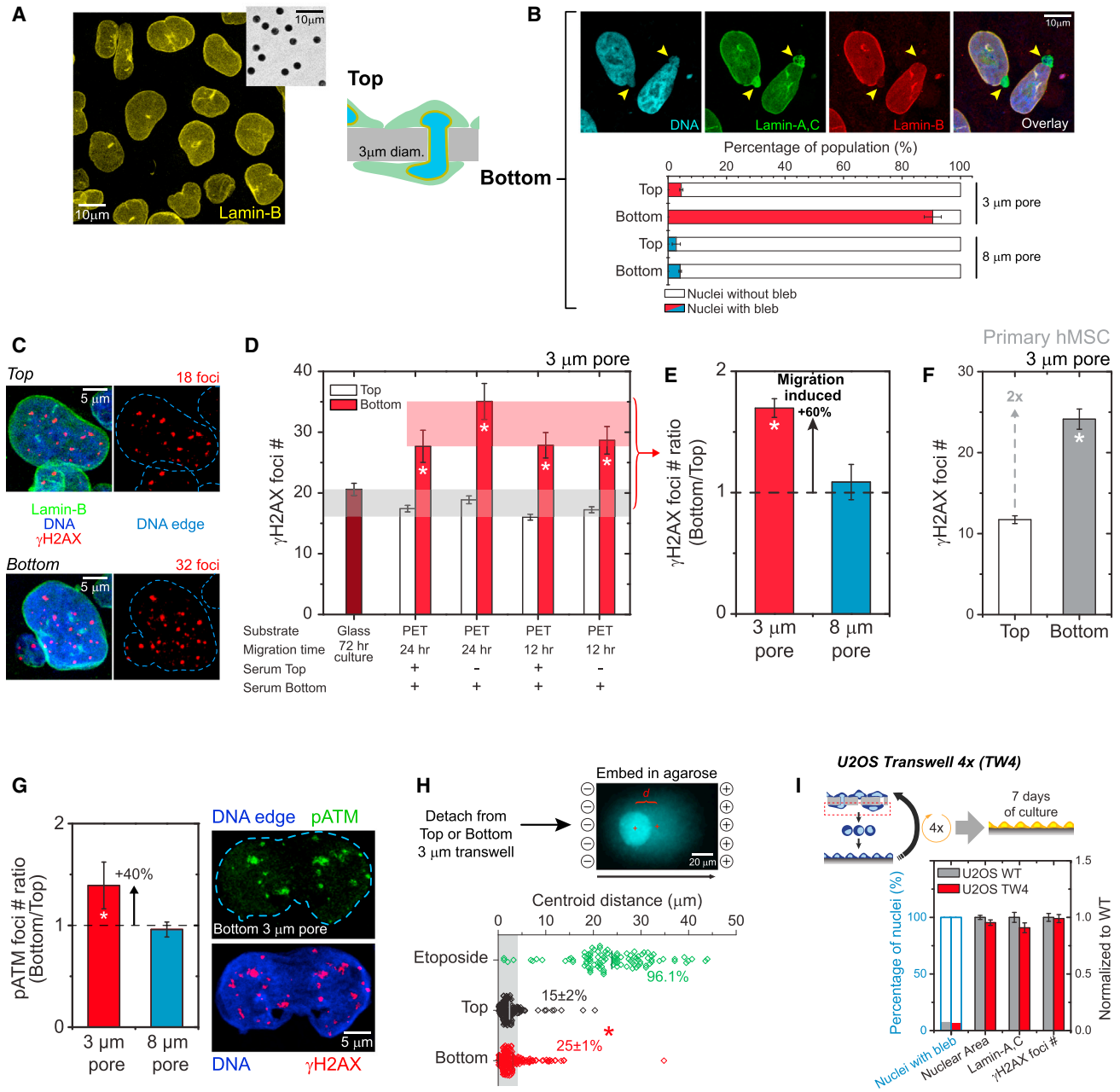

Figure 1. Migration through 3-μm Pores Causes Transient Nuclear Lamina Rupture, DNA Breaks, and Repair Factor Mis-localization

(A) U2OS nuclei on the tops of transwells are rounded (inset: 3-μm pores).

(B) Migration elongates and causes blebs on poles, but not with 8-μm pores. (Figure S1; ≥40 nuclei per condition, n ≥ 3 experiments, average ± SEM.)

(C–F) Immunostained γH2AX foci imaged on the tops or bottoms of transwells (C) or glass show increased damage after U2OS migration through 3-μm pores (D; PET, polyester), but not through 8-μm pores (E). Human mesenchymal stem cells (hMSCs) also show more foci after 3-μm pore migration (F). (Figure S1; ≥45 nuclei per condition, n = 3 experiments, average ± SEM, *p < 0.05.)

(G) Immunostained phospho-ATM (pATM) foci show increased damage after U2OS migration through 3-μm, but not 8-μm, pores. (≥50 nuclei per condition, n ≥ 3 experiments, *p < 0.05, average ± SEM.)

(H) Comet assay for DNA breaks in isolated U2OS nuclei show that 3-μm pore migration causes more centroid shifts (threshold: 3 μm), as does Etoposide in cultures (10 μM, 2 hr). (≥175 nuclei per group, n ≥ 3 experiments, average ± SEM, *p < 0.05.)

(I) Post-migration recovery of lamin-A,C, DNA damage, nuclear area, and blebs. (≥130 nuclei per condition, n ≥ 3 experiments, average ± SEM.)

cells pipetted into 96-well plates, and one clone was chosen (Ctrl_clone-1; Table S1) for si4 knockdown. The genomic homogeneity of 95.2% for this clone was determined from comparative genome hybridization arrays (aCGHs) that remain a "gold standard" for chromosome copy-number variations [34]. Imaging of metaphase chromosomes shows that si4 treatment gives

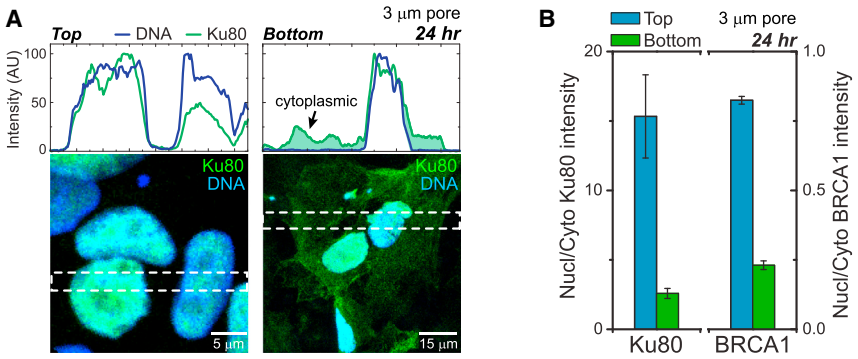

Figure 2. Constricted Migration Also Causes Repair Factors Mis-localization that Negatively Correlates with DNA Damage Levels

(A) Immunostained intensity profiles of repair factor Ku80 highlight nuclear localization on the top of 3-μm pores but cytoplasmic mis-localization on the bottom (green shade).

(B) For Ku80 and BRCA1, nuclear-to-cytoplasmic intensities decrease post-migration. (Figure S1; ≥10 fields of view per condition, n ≥ 3 experiments, average ± SEM.)

(C) Ku80 re-localizes over hours on the bottom as γH2AX foci count also decreases. (≥10 cells per condition, n ≥ 2 experiments, average ± SEM, *p < 0.05.)

more chromosomes (15–20 more) versus siCtrl and non-treated cells (Figure 3F*i*). The highest variation is with si4 treatment and is 3-fold greater than normal diploid MSCs, suggesting high genome variation and diverse aneuploidy within si4 cultures. All U2OS cells also exhibit much higher ploidy than MSCs, which is likewise evident in genomic analyses by aCGH (i.e., 41% more; Table S1). Fluorescence in situ hybridization (FISH) applied to Chr-1 (the longest is best for microscopy) shows the expected gains in copy number: comparing U2OS to MSCs (Figure 3F*ii*), Chr-1 segments are shorter and/or fused to other chromosomes but greater in total number (approximately eight versus four) and length (46% more). However, the lack of difference for Chr-1 between U2OS samples suggests that other chromosomes are likely to confer aneuploidy as caused by depletion of repair factors.

Changes in Chromosome Copy Number after Constricted Migration

Chromosome copy-number changes after constricted migration of U2OS cells seemed *possible* because (1) nuclear-to-cytoplasmic ratios of DNA repair factors are greatly decreased by migration (Figures 2A–2C) and (2) some of these factors when knocked out or mutated in mice cause changes in chromosome copy number [22–26]. In addition, we find that (3) partial, combined knockdown of multiple repair factors affects ploidy (Figures 3E and 3F) and increases DNA damage (Figures 3C and 3D). The genomes of U2OS cells were therefore analyzed before and after constricted migration, and we again used aCGHs (with clonality per Table S1). Single-nucleotide polymorphism array (SNPa) analyses and whole-exome sequencing (WES) were also used to further reveal chromosome copy-number changes that produce loss of heterozygosity (LOH). RNA sequencing (RNA-seq) was used to correlate transcript levels and genomic changes.

U2OS clones generated in standard 2D cultures done in parallel with a typical long-term, bulk culture of U2OS cells (Figure 4A) show heterogeneity in the latter (i.e., 87% clonality; Table S1). This is consistent with minimal genomic drift in long-term culture and migration on plastic [35]. Clonal expansion not only produces sufficient DNA for accurate genomic analyses, but also provides evidence of viable, proliferating cancer cells—typical of malignancy—versus non-viable or senescent cells with excessive DNA damage that might be analyzed by single-cell methods. Importantly, expansion from single U2OS cells can maintain high clonality for months in standard 2D cultures (>95%; Table S1). Furthermore, as expected from the high ploidy of U2OS cells (Figure 3F), aCGH and SNPa, as well as WES, consistently yield similar chromosome copy-number patterns across the genome of a given clone (Figures 4B, 4C, and S3), revealing three to four copies of many chromosomes (or parts of chromosomes).

Changes in chromosome copy number between any two samples were calculated as illustrated for Ctrl_bulk and Ctrl_clone-1 (Figure 4D). Heatmaps for easier visualization of the genome show gains (red), losses (green), and no change (black). Two different arrays (aCGH and SNPa) from different manufacturers have different probes, different standards, and different genome coverage, but the heatmap from the "gold standard," aCGH [34] is largely the same as that from SNPa analyses (Figure 4D). SNPa analyses yield additional, highly accurate information on loss of heterozygosity (LOH; which indicates complete loss of either "mother" or "father" derived alleles), and the relatively rare LOHs are summarized by red or green tick marks against a light background beneath chromosomal heatmaps (Figure 4D). LOH differences are low (~10 Mb) for control cells that proliferate on plastic for weeks.

A clone that is genomically 100% homogeneous based on aCGHs was subjected to three rounds of constricted migration through transwells (TW3), and for genomic analyses single-cell clones were once again isolated and expanded from the migrated population by 96-well serial dilution (Figure 4E). Three

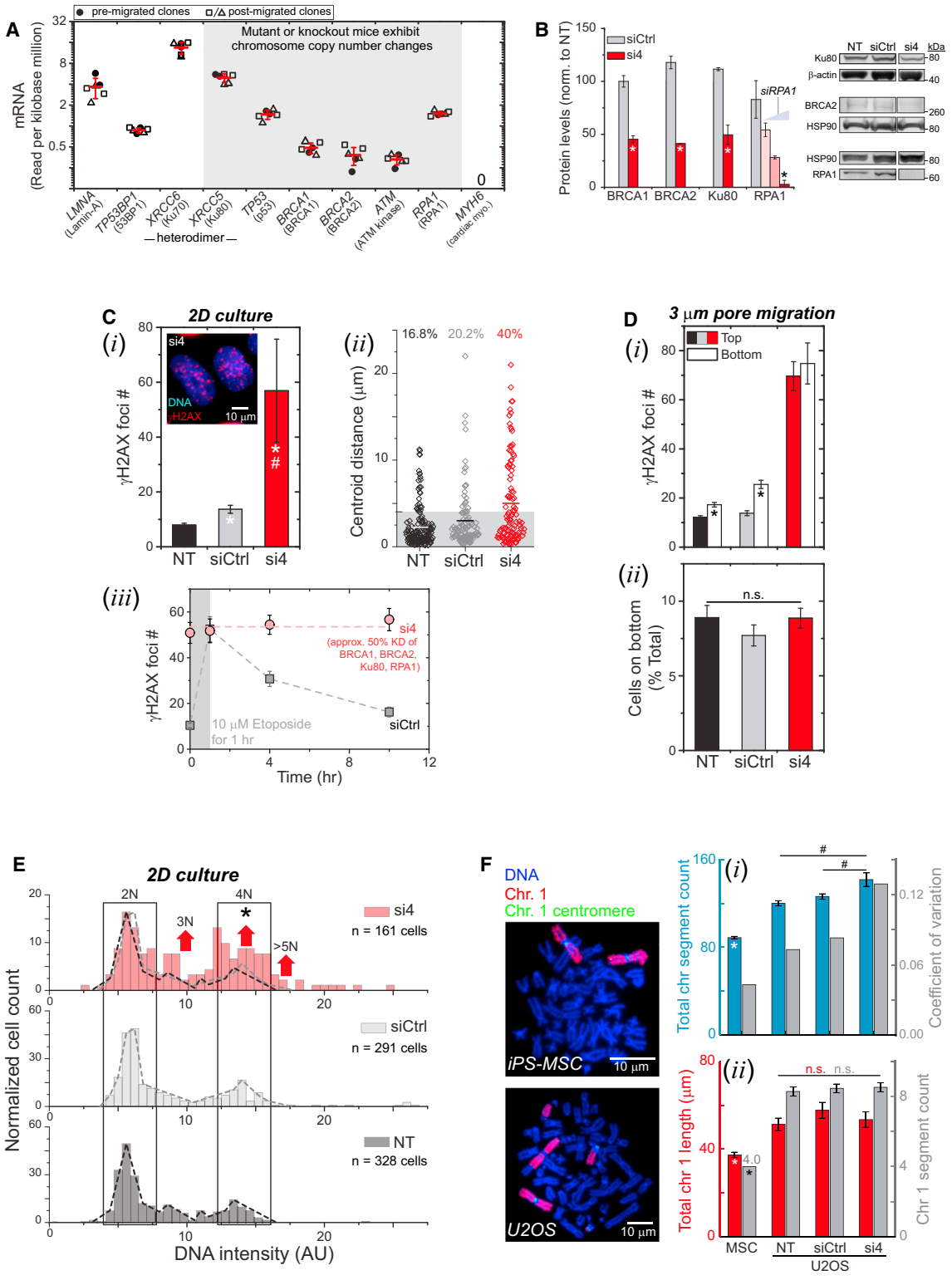

Figure 3. Partial Depletion of Multiple Repair Factors Leads to DNA Damage Accumulation and Chromosomal Variation

(A) Key nuclear or DNA repair transcripts from RNA-seq analysis of U2OS cultures, either pre- or post-migration. Mouse knockouts or mutations of key genes cause copy-number variations. *MYH6* (a cardiac specific gene) shows zero reads. (Normalization to reads per kilobase million, n = 8 samples, average ± SD.)

(legend continued on next page)

rounds of 3-μm migration were chosen because a single round generated minimal genome variation (Figure S3). Subtraction of the starting clone's genome from genomes of the triply migrated TW3 clones reveals unique gains and/or losses in parts of many chromosomes (Figure 4F, white asterisks and blue bars). Changes in chromosome copy number can total hundreds of megabases (clones 5 and 6), which differ significantly from less affected clones (Figure 4G).

A subset of the chromosome changes in clones 3 to 6 also involved the gain and/or loss of LOH regions (Figure 4F). The significant anti-correlation of LOH with changes in chromosome copy number (Figure 4H) indeed confirms that a gain or loss of LOH associates tightly with a respective loss or gain of a chromosome segment. LOH gains exceed LOH losses for a given sample (also in the data of independent experiments below), and the low LOH losses could reflect either a low-frequency process of DNA mis-repair or else measurement uncertainties (see below). Constricted migration of a 100% clonal population can thus give rise to genomic variation.

A standard 2D bulk U2OS culture (from Figure 4A) was also subjected to pore migration, with distinct single-cell clones isolated after three rounds (TW3) and seventeen rounds (TW17) of migration (Figure 5A). Starting with a non-clonal "bulk" culture (87% clonal) is important for assessing whether statistically significant genome heterogeneity can be added to a standard cell culture, which seems typical of tumors that become multi-clonal (e.g., osteosarcoma) [15]. In order to control for passage number, we performed transwell migrations in parallel to the 2D culture: clonal selection (in 96-well plates) and DNA isolation for TW3 and non-migrated controls were thus done at the same time. Subtraction of pre-migration "bulk" (Ctrl_bulk of Figure 4B) to generate heatmaps (per Figure 4D) reveals partial gains and losses in chromosome copy numbers (Figure 5B), and although the control clones differ the least in clustering together, all clones exhibit uniqueness. TW3_clone-2 shows a unique loss of one copy of Chr-1p from three to four copies of this arm in Ctrl_bulk (or any control clones; Figure 4B). TW17_clone-1 shows a unique loss of Chr-10p plus half of Chr-10q from three to four copies in control clones. WES of key samples shows the same trends (Figure S4).

Quantitation of chromosome copy number from the heatmaps indicates greater loss of hundreds of megabases for TW3s on average compared to control clones (Figure 5C). TW17s show more gains relative to TW3s and control clones (Figure 5C). LOH changes are again a small subset of anti-correlated changes in chromosome copy number (Figure 5D) and arise again from losses in many more chromosomes compared to gains (Figure 5E), suggestive of typical LOH mechanisms [36]. Changes in single-nucleotide variations (SNVs) largely overlap with changes in LOH (Figure S4) and compared to control clones the TW17 clones show many more SNVs (Figure S3). Pairwise analyses of SNVs in additional control clones further show minimal variation, as expected of clonality (Figure S3), whereas variation increases with rounds of migration to the highest levels between TW17 clones. Clones thus diverge genomically with migration.

Changes in LOHs of each chromosome were also checked as SNVs (Figure S3): LOH gains mostly coincide with SNV calls, but LOH losses do not. For a high-confidence measure of heterogeneity of TW3s generated in the two experiments (i.e., six clones in Figures 4E–4H from one clone, and three clones in Figures 5A–5E from bulk), pairwise differences were determined for SNV-confirmed LOHs (as total megabases = mostly gains + a few losses), and the mean ΔLOH was calculated across all pairs. The two experiments above plus a third quantify ΔLOH variations (Figure 5F), which reflect both chromosome copy-number changes and SNV coincidence. The third experiment also included TW3 clones generated by migration through larger, 8-μm pores. Although large pores cause minimal nuclear blebbing and DNA damage (Figure 1), ATMi toxicity increases inversely with pore diameter relative to 2D cultures (Figure S2). LOH heterogeneity is nonetheless greatest for 3-μm pores.

RNA-seq analyses of many samples above were once again compared to Ctrl_clone-1. Zero reads of mRNA from the Y chromosome (Table S2), in addition to zero LOH and SNV calls, are consistent with derivation of the U2OS line from a female patient; in contrast, 40%–57% of genes from all other chromosomes are expressed. Fold changes in transcript (1 Mb averaged) from this fourth "omic" method were mapped to changes in chromosome copy number (Figures 5G and S4). Most transcript changes correlated with changes in gene copy number ($p << 0.01$; Figure 5G; Table S3), per expected "gene dosage" effects [37].

For DNA repair factors that can cause variations when mutated (Figure 3A), TW3_clone-3 shows no mRNA deficiencies, and so its genome variations are not explained by defects in these repair factors. ATM mRNA is low in three migrated clones, but ATM inhibition does not affect DNA damage in U2OS cells (Figure S2). However, TW3_clone-1 shows a decrease by half of Ku80 that could suffice to increase DNA damage in this one clone (Figure S2). A 2-fold decrease in BRCA2 in Ctrl_clone-3

(B) Simultaneous partial knockdown of four repair factors (si4; red) versus control (siCtrl; gray) when normalized to non-treated (NT). For each siRNA (red), 25 nM was used, except for siRPA1 titration (Figure S2). Protein levels quantified by immunoblots were normalized by housekeepers (HSP90 and beta-actin), with BRCA1 quantified by immunofluorescence. ($n = 3$ blots or $n \geq 150$ nuclei, $n = 3$ experiments, average ± SEM, $^{*}p < 0.05$.)

(C) DNA damage increased in 2D cultures of si4 cells based on γH2AX foci (*i*; Figure S2) and comet assay (*ii*). siCtrl slightly increases damage, perhaps because of lipofectamine. DNA damage sites induced by 1 hr 10 μM etoposide treatment are resolved by the siCtrl cells within hours, but γH2AX foci count of si4 cells remained at a high number (*iii*; ≥110 nuclei per condition, $n \geq 3$ experiments, average ± SEM, $^{*}p < 0.05$ versus NT, $^{\#}p < 0.001$ versus siCtrl).

(D) si4 increases γH2AX foci regardless of 3-μm pores migration, whereas damage increases in controls (*i*; ≥50 nuclei per condition, $n \geq 3$ experiments, average ± SEM, $^{*}p < 0.05$ between top and bottom). Migrated percentages are similar for all conditions (*ii*; Figure S2; ≥3 transwells per condition, $n \geq 3$ experiments, average ± SEM).

(E) DNA content from Hoechst-33342 intensity shows 2N and minor 4N peaks for controls but shifts for si4 indicate poly- or aneu-ploidy (Figure S2; ≥160 nuclei per condition, $n \geq 3$ experiments, average ± SEM; $^{*}p < 0.001$ in a two-sample Kolmogorov-Smirnov [KS] test for higher modes, with $\alpha = 0.05$ [27]).

(F) Metaphase spreads show higher ploidy of U2OS cells versus diploid MSCs and more chromosome segments for si4 cells (*i*). Both Chr-1 length and segment counts of U2OS are higher versus MSCs, but (*ii*) Chr-1 counts are unaffected by si4 (≥20 spreads per condition, $n \geq 3$ experiments, average ± SEM, $^{*}p < 0.05$ MSC versus U2OS, $^{\#}p < 0.05$ U2OS versus U2OS).

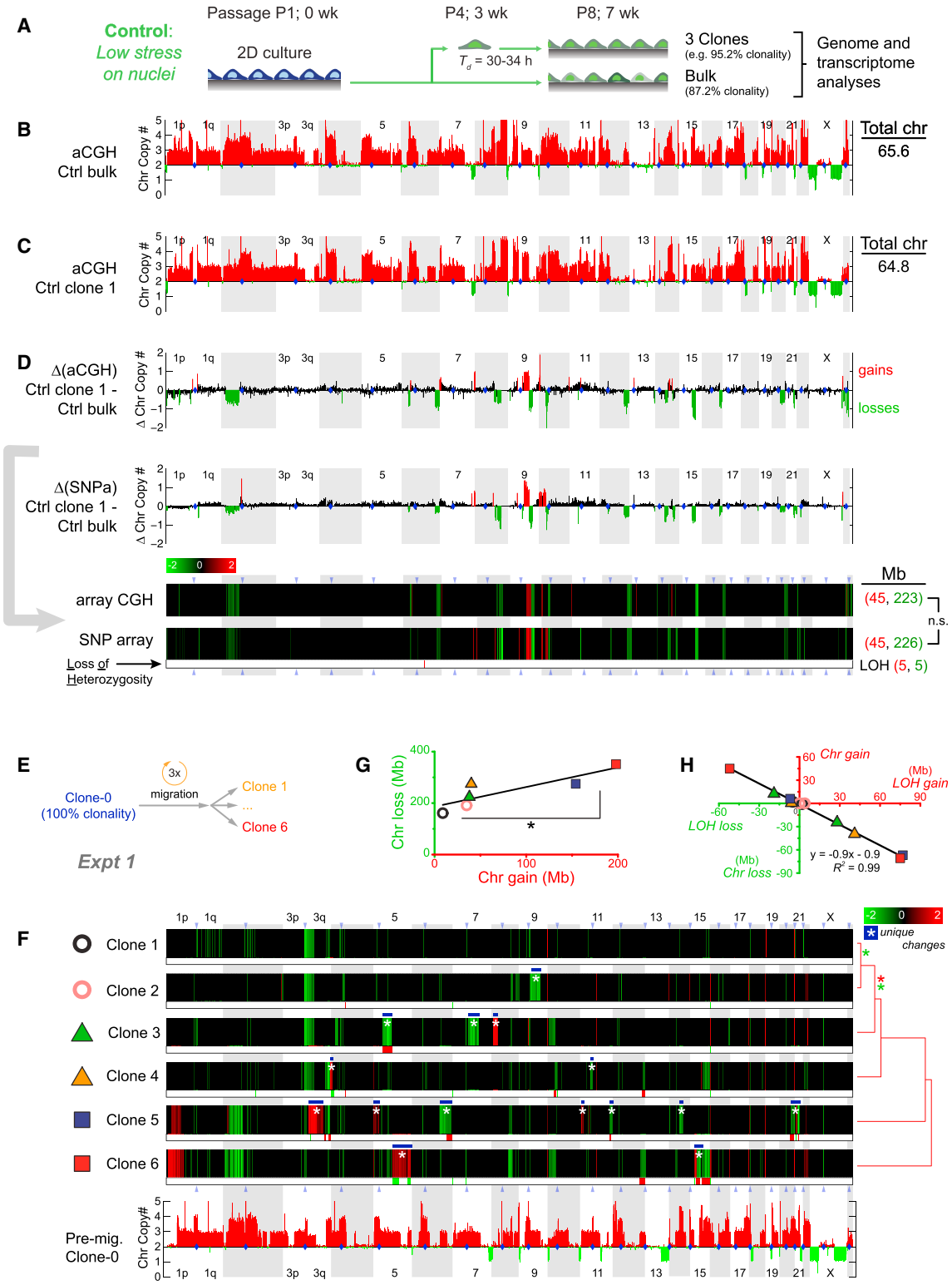

Figure 4. Constricted Migration Introduces Genomic Variation

(A) U2OS culture with 87.2% clonality (Tables S1 and S6) diluted to single cells in 96-well plates to generate control clones. Genomic analyses included aCGHs and SNPa analyses.

(B and C) Chromosome copy numbers from aCGHs for bulk U2OS (Ctrl_bulk; B) and one clone (Ctrl_clone-1; C; Figure S3). Total chromosome numbers are calculated per Table S2.

(legend continued on next page)

is perhaps consistent with deficits reported for U2OS [15], and a lack of correlation with chromosome copy number merely illustrates alternative, epigenetic regulation [38]. Because low expression of key repair factors is otherwise rare, depletion of nuclear pools for many hours after nuclear rupture remains a better explanation for DNA damage in constricted migration (Figure 1).

Phenotypic Changes Reflect Genomic Changes

Proliferation rates of all clones generated after migration appeared similar (Figure S5), which is sensible because constricted migration seems unlikely to select for proliferation. However, while we were imaging cells for cell counts of various clones, TW17_clone-2 appeared distinctly spindle shaped. A *k*-means clustering analysis of mRNA levels showed that 1,789 genes were uniquely up in this clone (Figure 6A). Chromosome maps (Figure 5B) also show that this clone has unique gains in Chr-6q and Chr-8p, corresponding to 191 genes for which we have RNA-seq results: 76% of these transcripts (145 genes) are up per gene dosage (Figure 5G). Functional analyses of the many transcript changes (by DAVID Bioinformatics 6.7 [39]) reveal enrichment for the microtubule (MT) cytoskeletal system only in TW17_clone-2.

MT organization has long been associated with cell morphology and polarity [40], and MTs span the long axis of prototypical spindle-shaped MSCs (Figure S5). The elongated aspect ratio of most TW17_clone-2 cells propagates with further cloning (Figures 6B and S5). Elongated cells with aspect ratio >5 are extremely rare in cultures of the other clones (1% ± 1%), and given that we randomly chose only three TW17 clones, selection of such rare elongated clones is unlikely ($p < 0.05$). High clonality (Table S1) also makes selection unlikely. An elongated shape is thus a likely consequence of genomic changes caused by migration. Importantly, nocodazole-induced depolymerization of MTs in TW17_clone-2 decreases cell aspect ratios to a level similar to rounded clones (Figure 6C*i*), confirming a key role of MT assembly in an elongated shape.

In scanning the 145 genes on Chr-6 or Chr-8 that are uniquely upregulated in TW17_clone-2, we noted an ~2-fold upregulation of *GATA4* (Figure 6A), which is a transcription factor that drives an endothelial-to-mesenchymal transition (EMT) process in cardiogenesis where—more specifically—GATA4 repression decreases MT-associated proteins [41]. Cardiac genes such as cardiac myosin are not expressed in U2OS cells (Figure 3A), but GATA4 maintains osteoblast progenitors [42], which often originate from MSCs [43]. GATA4 inhibits osteogenic differentiation [44] and is relevant to the osteosarcoma origin of U2OS cells.

Averaging all genes within 1 Mb of GATA4 confirmed its significant upregulation only in TW17_clone-2 (Figure 5G). If high levels of GATA4 in this clone (Figure 6A) suffice to drive the spindle shape, then (1) GATA4 knockdown in TW17_clone-2 (Figure S5) should decrease the aspect ratio and (2) GATA4 overexpression in a rounded clone (Figure S5) should drive elongation. These predictions hold true (Figures 6C*ii* and 6C*iii*) and even yield the expected shape distributions (Figure 6D). Spindle-shaped U2OS cells show MTs from end to end, consistent with MSCs and morphological roles (Figure S5). The elongated clone also migrates more efficiently through pores unless treated with siGATA4 (Figures 7A and 7B), although migration-induced DNA damage still occurs (Figure 7C).

DISCUSSION

Constricted migration increases the number of DNA damage foci (based on three independent approaches) and depletes DNA repair factors for hours (Figures 1 and 2). Partial knockdown of such factors in 2D cultures delays DNA repair by at least hours and increases both damage and chromosome aberrations (Figure 3). Damage foci are nucleoplasmic (Figure S1), consistent with repair factor loss (Figure 3) but contrasting with GFP-53BP1 foci at the distal end of a migrating nucleus [3] and also contrasting with DNA damage just at the leading edge of the nucleus [7]. Chromatin fragmentation as a nucleus enters and elongates in a small pore was separately considered as a mechanism for increasing breaks but seems unlikely because stretched chromatin maintains its integrity even if cleaved by a nuclease [45].

Constricted migration of U2OS clones additionally causes many unique gains and losses in large segments of chromosomes in diverse clones (Figures 4 and 5), consistent with copy-number variations in mouse mutants of some DNA repair factors [22–26]. Although clonality of U2OS cells can be reasonably maintained in 2D culture (Table S1), constricted migration could simply be amplifying deficient repair pathway(s) that explain the multi-clonality in osteosarcoma tumors [13, 14]. Nuclear entry of DNA-damaging nucleases has also been speculated [3, 7], but evidence in osteosarcomas is lacking. Moreover, the pan-nucleoplasmic distribution of DNA damage foci (Figure 1) would require exclusion of non-specific nucleases that would tend to damage DNA primarily near the site of envelope rupture. TREX1 nuclease can indeed cause damage that seems to be locally restricted to fully exposed DNA [46]: a TREX1-positive chromatin bridge between two dividing cells (with co-localized RPA repair complex) perforates the nuclear envelope to cause massive release of mobile factors, including GFP-NLS- and GFP-RPA1-type constructs, but immunofluorescence suggests no effect on TREX1 nucleoplasmic levels. Quantitative imaging (per Figures 1 and 2 here) with knockdown and

(D) Differences in chromosome copy numbers between Ctrl_bulk and Ctrl_clone-1 are heatmapped as changes in chromosome copy numbers (ΔChr copy#). Gain (red) and loss (green) calls in aCGH data were thresholded at ±0.48 based on ΔChr copy# distributions from all pairwise comparisons in Table S1. Ctrl_clone-1shows more net losses and fewer chromosomes. Gain and loss calls for this SNPa comparison were thresholded at +0.6 and −0.2 to match gains and losses of aCGHs, and KS tests (Figure 3E) show no difference between gain distributions and between loss distributions. SNPa also shows few LOHs (below the heatmap).
(E) 100% clonal U2OS after three migrations through 3-μm pores was used to make six single-cell-derived clones for SNPa analyses.
(F) Compared to pre-migration clone-0, migration causes unique ΔChr copy# (white asterisks) and LOHs. Clones are listed per hierarchical clustering (city-block metric) of their ΔChr copy#, and asterisks indicate statistical significance ($p < 0.05$ in KS tests) between the distributions of gains (red asterisk) or distributions of losses (green asterisks). Gain and loss calls were thresholded at ±0.42 based on aCGH versus SNPa (see the Experimental Procedures).
(G) Chromosome gains and losses reach hundreds of megabases, and two clones (5 and 6) show the highest gains (*$p < 0.05$).
(H) LOHs anti-correlate with chromosome copy-number changes.

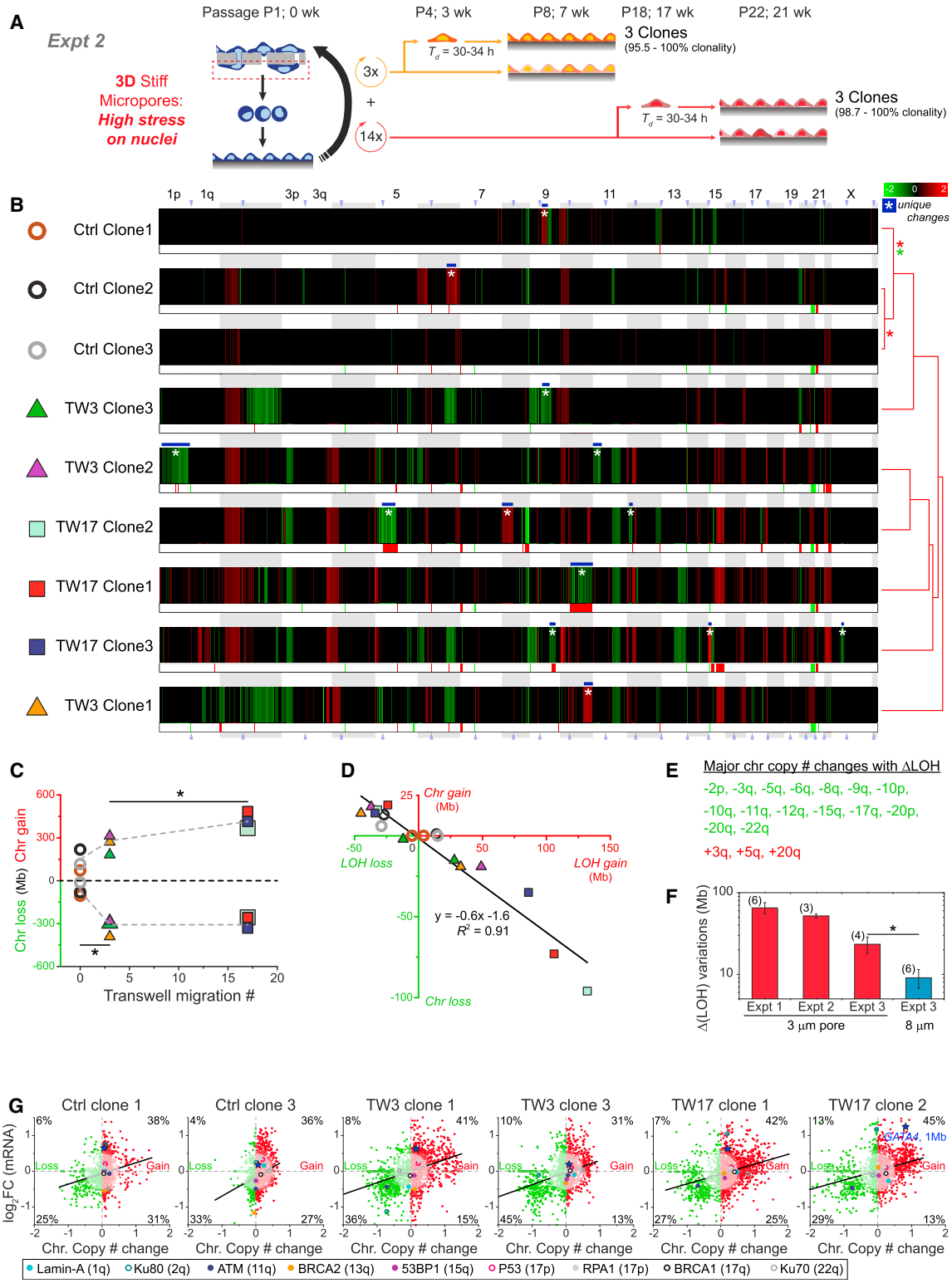

Figure 5. More Migration Causes More Genomic Variation, with Changes Evident in Expression

(A) Migration of "bulk" U2OS for three (TW3) or seventeen (TW17) rounds was followed by clonal expansion (Table S1), SNPa, and RNA-seq analyses. To control for genomic variation in culture, we passaged TW3 and Ctrl clones in parallel.

(B) Relative to pre-migration "bulk," ΔChr copy# shows Ctrl clones cluster together versus migrated clones, which all show many more ΔChr copy#, with many unique changes (white asterisks). ΔLOH regions were greatest in TW17 clones. Clones are listed per hierarchical clustering (city-block metric) of their ΔChr copy#,

(legend continued on next page)

overexpression of nucleases such as TREX1 should of course be combined with genomic analyses of expected chromosome changes [46]. Regardless, damage to DNA will increase through any damage-favoring imbalance between damage factors and repair factors.

Mechanisms of migration-induced increases in DNA damage based on loss of repair factor(s) seem both similar to and different from mechanisms elaborated for lamin-A-null fibroblasts in standard cultures [6]. Repetitive rupture of the nuclear envelope in such cultures on rigid surfaces causes cytoplasmic mis-localization of multiple mobile nuclear factors [47] (which is minimized on soft, tissue-like substrates that reduce nuclear stress [48]); 53BP1 protein is thus expected to be more cytoplasmic, which could explain its rapid degradation in lamin-A-null fibroblasts in the absence of any transcript change [6]. Importantly, overexpression of 53BP1 has proven sufficient to rescue some forms of DNA damage in lamin-A-low cells [6]. Loss of 53BP1 likewise occurs early across many human cancers of different tissue and cell types, but it occurs more consistently than appearance of γH2AX [49], which suggests decoupling from 53BP1. Indeed, in constricted migration of U2OS cancer cells that have abundant lamin-A (Figure 1) and pre-existing cancerous changes (Figure 3), overexpression of 53BP1 is not sufficient to reproducibly provide a significant rescue (Figure S1). Mis-localization after migration is, however, transient for repair factors (Figures 1 and 2) that are known to regulate chromosome copy-number variations—including BRCAs that explain genomic aberrations in osteosarcoma [15]. The fact that lamin-A is highly mutated but does not increase the risk for cancer (unlike mutations in repair factors such as BRCAs) further implicates other important mechanisms unrelated to rupture, such as squeezing-dependent segregation of repair factors away from chromatin [21]. Lastly, although mechanistic links between our main observations of DNA damage, repair factor depletion, and genome variation might benefit from more direct comparisons with the effects of lamin-A depletion and rescue with multiple repair factors, the EMT-like change in cancer cell phenotype after migration (Figures 6 and 7) illustrates invasion-mutation mechanisms pertinent to metastasis and the heterogeneity within and between tumors [50].

EXPERIMENTAL PROCEDURES

Cell Culture

U2OS, an osteosarcoma cell line, and A549, a human lung adenocarcinoma cell line, were cultured in DMEM high-glucose media and Ham's F12 nutrient mixture (GIBCO, Life Technologies), respectively, supplemented with 10% fetal bovine serum (FBS) and 1% penicillin and streptomycin (Sigma-Aldrich). MSCs were cultured as described previously [2].

Transwell Migration

For migration through transwells (Corning), cells were seeded at 300,000 cells/cm^2 onto the top side of the filter membrane and left to migrate in normal culture condition for 24 hr. The number of migrated cells on the bottom is proportional to the number of cells added on the top in a given set of experiments, and so different experiments are readily compared by normalizing to a control sample such as non-treated. For isolation of the cells from the transwell, cells were detached from the transwell by using 0.05% Trypsin-EDTA (GIBCO, Life Technologies). If the isolated cells were to undergo another transwell migration, they were expanded for 1 week to reach the required number of cells. Alkaline comet assays of the migrated cells were carried out per manufacturer's instructions (Cell Biolabs). Image processing to determine the centroid of main nuclear body and its comet tail was done in MATLAB (MathWorks). Intensity thresholding was used to locate the comet area, whereas distribution of the intensity derivatives was used locate the main nuclear body area. The centroids were calculated from the area locations.

Genome and Transcriptome Analysis

DNA isolation used the Blood and Cell Culture DNA Mini Kit (QIAGEN) per the manufacturer's instructions. Chromosome copy number was measured using the aCGH SurePrint G3 Human Genome CGH+SNP Microarray 4×180k (Agilent), which involves ~110,000 probes for CGH and ~60,000 probes for SNP detection. Isolated DNA samples were shipped to Cell Line Genetics for aCGH measurements. Cell Line Genetics used standard CytoGenetics (Agilent) to provide a summary analysis and raw data for each sample; see Table S4 for a representative summary report and raw data table from aCGHs (the data files are large, but all raw data are available for review at any time). In addition to the sample clonality (as indicated by "clonal fraction" in Table S4), raw data indicate regions of both chromosome copy-number and LOH variation. Further analyses were done with custom algorithms written in MATLAB. For validation of aCGH results, the same DNA samples were also sent to The Center for Applied Genomics Core in The Children's Hospital of Philadelphia for the SNPa HumanOmniExpress-24 BeadChip Kit (Illumina). For this array, >700,000 probes have an average inter-probe distance of ~4 kb along the entire genome. For each sample, the Genomics Core provided the data in the form of GenomeStudio files (Illumina). Chromosome copy number and LOH regions were analyzed in GenomeStudio with the cnvPartition plugin (Illumina). Regions with one chromosome copy number are not associated with LOH by the Illumina's algorithm. Hence, regions with one chromosome copy number as given by the GenomeStudio are added to the LOH region lists. Comparison analyses between SNPa and aCGH were again done in MATLAB. SNP array experiments also provide genotype data, which was used to give SNV data. Genotyping in this Illumina system relies on the correlation between total intensity and intensity ratio of the two probes, one for CG and another for AT. These correlations were mapped to a standard clustering file (Illumina) to give the SNP calls. In order to compare different samples, probes with "no call" (either due to low read intensity or located outside the "call" cluster) were removed from further analysis. In order to increase the confidence of LOH data given by the GenomeStudio, the changes in LOH of each

and asterisks indicate significance ($p < 0.05$ in KS tests) between the distributions of gains (red asterisks) or distributions of losses (green asterisk). Gain and loss calls for these samples were thresholded per Figure 4F. Table S3 compares samples to Ctrl_clone-1 and leads to similar conclusions of genome variation.

(C) ΔChr copy# reached hundreds of megabases and increased with rounds of migration (*$p < 0.05$, Student's t test).

(D) LOHs and ΔChr copy# anti-correlate per Figure 4H.

(E) Major ΔChr copy# (loss green; gains red) that show changes in LOH.

(F) ΔLOH variations within samples of independent TW3 experiments were derived from pairwise comparisons of changes in SNV-confirmed LOHs, with means calculated for all pairs. Experiment 1 is from Figures 4E–4H migration of a clone, experiment 2 is from Figures 5A–5D migration of bulk, and experiment 3 involves four more 3-μm TW3 clones and six 8-μm TW3 clones migrating from a bulk culture (Figure S3). Even though ΔLOH variations were observed within all groups, consistent with heterogeneity, variation for 3-μm pores always exceeds that for 8-μm pores (average ± SEM, *$p < 0.05$).

(G) Transcript changes (RNA-seq) correlate with ΔChr copy# from SNPa analyses (1 Mb averaging for both datasets; Table S3). Data within the white oval have $\log_2$(RNA_ratio) and ΔChr copy# < 0.5. For significance tests, the thresholded percentage of data in the upper right and lower left versus the lower right and upperleft was calculated for all plots: $p = 5 \times 10^{-6}$ (Tables S4 and S5). Genomic heatmaps of RNA-seq data aligned with the ΔChr copy# are shown (Figure S4). The blue star indicates a 1-Mb window containing *GATA4*, and colored circles indicate 1-Mb windows containing nuclear factors of Figure 3A.

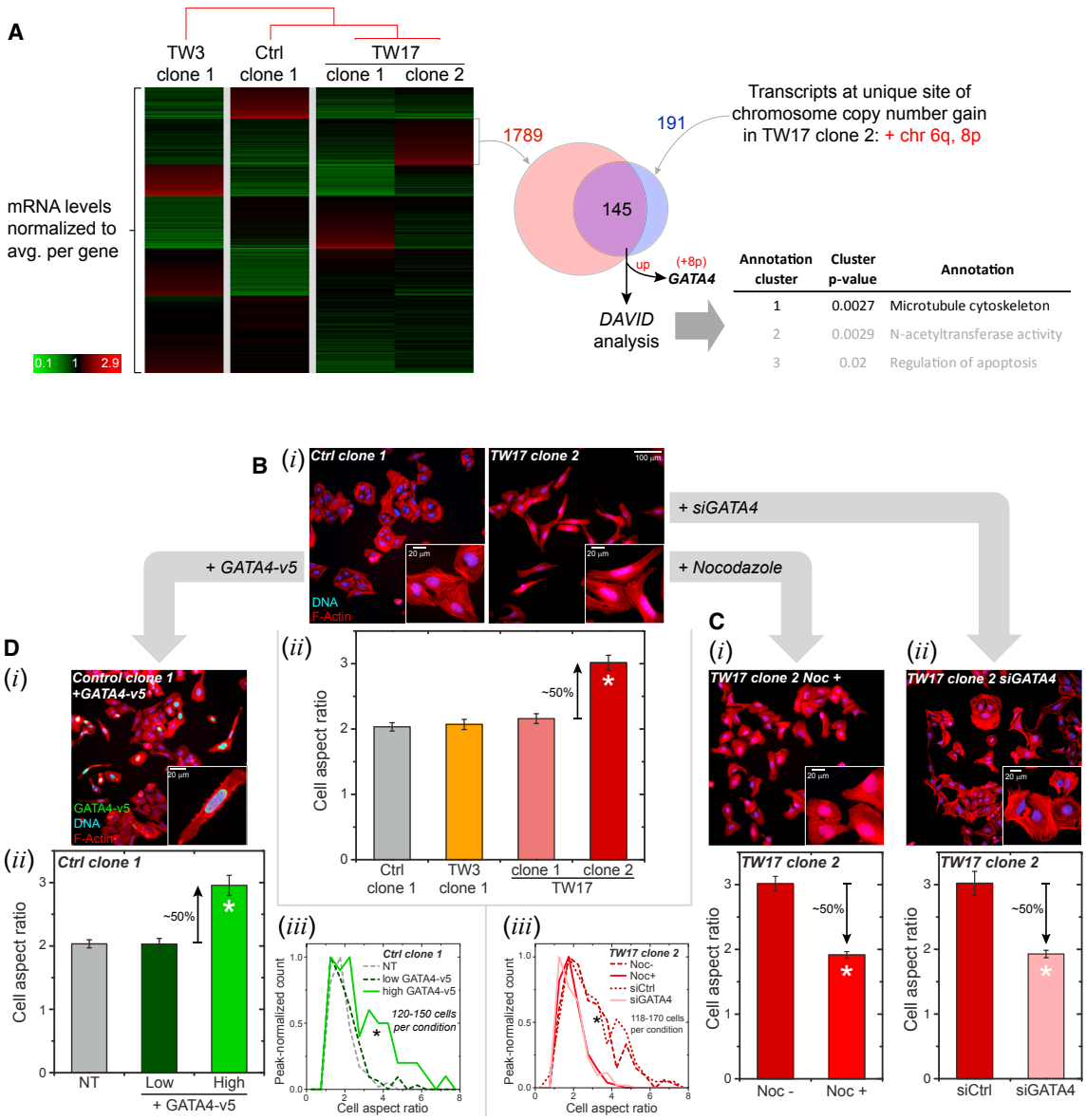

Figure 6. Phenotypic Changes Driven by Migration-Induced Genome Variations

(A) mRNA from four clones (Ctrl_clone-1, TW3_clone-1, TW17_clone-1, and TW17_clone-2) was normalized by the average value for each gene. *k*-means clustering applied to the transcriptome data revealed a transcript cluster uniquely upregulated in TW17_clone-2 (1,789 genes). Clones are listed per hierarchical clustering (city-block metric) of transcript levels. Only two chromosome gain regions are unique to TW17_clone-2: Chr-6q and Chr-8p. These unique regions correspond to 191 transcripts in the RNA-seq data, with 145 genes being upregulated. Functional annotation analysis (DAVID Bioinformatics 6.7) reveals enrichment of the MT cytoskeleton, suggestive of MT upregulation in TW17_clone-2. *GATA4* also resides in Chr-8p and is in the overlap list. Similar comparisons with all samples in Figure 5 yield Chr-8p as the only unique chromosome gain region and give 107 overlapping genes, with the MT cytoskeleton statistically enriched and *GATA4* listed.

(B) Cell aspect ratio from F-actin staining by phalloidin (*i*) calculated from major over minor axes (*ii*). Higher aspect ratios were observed only for TW17_clone-2, indicating more elongated cells (Figure S5; ≥150 cells per condition, n ≥ 3 experiments, average ± SEM, *p < 0.05).

(C) De-polymerization of MTs with 10 μM nocodazole and GATA4 depletion by siGATA4 (Figure S5) on TW17_clone-2 leads to more rounded cells with a decreased aspect ratio (*i* and *ii*) and shifts in aspect ratio distributions (*iii*) (≥140 cells per condition, n ≥ 3 experiments, average ± SEM, KS tests *p < 0.05).

(D) Overexpression of GATA4-v5 in Ctrl_clone-1 elongates cells (*i*) per higher aspect ratio (*ii*; Figure S5), shifting the aspect ratio distribution (*iii*; ≥120 cells per condition, n ≥ 3 experiments, average ± SEM, KS tests *p < 0.05). Anti-v5 identifies expressing cells.

chromosome from each sample were cross-referenced to their corresponding SNV data.

The isolated DNA samples were sent to the Next-Generation Sequencing Core at the Perelman School of Medicine, University of Pennsylvania, for exons capture by using SureSelect Clinical Research Exome kit (Agilent), per the manufacturer's standard protocol. Three samples were pooled together and submitted to HiSeq 2500 (Illumina) for 100-bp paired-end sequencing, resulting in ~80,000,000 reads for each sample. Chromosome copy-number analysis was done with the CNVkit software package (https://media.readthedocs.org/pdf/cnvkit/latest/cnvkit.pdf).

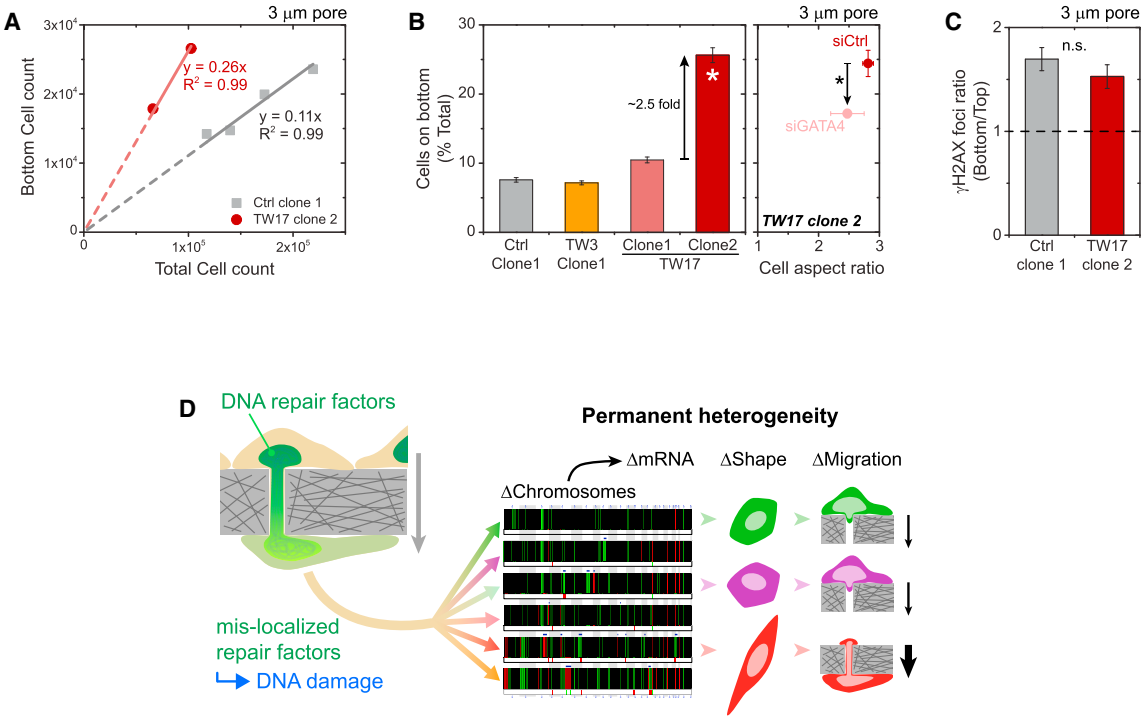

Figure 7. Clone with Elongated Morphology Migrates More Rapidly, but Migration Still Increases DNA Damage

(A) TW17_clone-2 squeeze through 3-μm pores in greater numbers than other clones, with a greater proportion of cells on the bottom (≥3 transwells per condition, n ≥ 3 experiments, average ± SEM, *p < 0.05).

(B) siGATA4 treatment leads to lower number of migrated cells, and the cell aspect ratio of the migrated siGATA4 cells tends to be lower (≥125 cells per conditions, n ≥ 3 experiments, average ± SEM, *p < 0.05).

(C) TW17_clone-2 is still prone to migration-induced DNA damage (≥50 cells per condition, n ≥ 3 experiments, average ± SEM).

(D) Overall, cell migration through micron-size constrictions causes transient mis-localization of DNA repair factors and thereby causes DNA damage, which leads to permanent heterogeneity in chromosome copy numbers, expression levels, cell shape, and migration capability.

RNA isolation used the RNeasy plus Mini Kit (QIAGEN). For RNA-seq analyses, RNA samples were also sent to the Next-Generation Sequencing Core. Libraries for RNA-seq were made with the TruSeq Stranded mRNA Library Prep kit (Illumina) per manufacturer's instructions, followed by 100-bp paired-end sequencing with HiSeq 2500. Ten cDNA libraries were pooled together, resulting in ~16,000,000 reads for each sample. Reads per kilobase million for each gene were calculated by normalization of the read of each gene by the sample's total read count (in millions) and by the gene length (in kilobases). Data processing and clustering were done in MATLAB, and function annotation analyses were done with DAVID Bioinformatics 6.7 [39].

Immunostaining and Imaging

Transwell membrane was fixed in 4% formaldehyde (Sigma) for 15 min, permeabilized by 0.25% Triton-X (Sigma) for 10 min, blocked by 5% BSA (Sigma), and incubated overnight in various primary antibodies: lamin-A/C (Santa Cruz and Cell Signaling), lamin-B (Santa Cruz), γH2AX (Millipore), Ku80 (Cell Signaling), BRCA1 (Santa Cruz), BRCA2 (Milipore), RPA1 (Santa Cruz), phosphorylated S1981 ATM (Abcam), α/β tubulin (Cell Signaling) and v5 (Abcam). Finally, the primary antibodies were tagged with the corresponding secondary antibodies for 1.5 hr (ThermoFisher). For F-actin staining, 100 ng/mL TRITC-phalloidin (Sigma-Aldrich) was also added to the secondary antibody solution. DNA was stained with 8 μM Hoechst 33342 (ThermoFisher) for 15 min. When mounting is involved, Prolong Gold antifade reagent was used (Invitrogen, Life Technologies). Epifluorescence imaging was performed using an Olympus IX71 with a digital EMCCD camera (Cascade 512B, Photometrics) and a 40×/0.6 NA objective. Confocal imaging was done in Leica TCS SP8 system with either a 63×/1.4 NA oil-immersion or 40×/1.2 NA water-immersion objective. Various image quantifications and processing were done with either ImageJ or MATLAB.

Protein Modulation in U2OS Cells

The small interfering RNAs (siRNAs) used in the main study were purchased from Dharmacon (ON-TARGETplus SMARTpool siBRCA1, L-003461-00; siBRCA2, L-003462-00; siKu80, L-010491-00;siRPA1, L-015749-01; and non-targeting siRNA, D-001810-10). For specificity validation (Figure S2), additional siRNAs were purchased from ThermoFisher (Silencer Select siBRCA2 s2085, siKu80 s14953, siKu80 s14954, and siRPA1 s12127), and siBRCA1 (5′-AGAUAGUUCUACCAGUAAA-3′). U2OS cells were passaged 24 hr prior to transfection. Pooled siRNA oligos (25 nM; four siRNAs/target) and 1 μg/mL Lipofectamine 2000 were prepared according to the manufacturer's instructions and incubated for 24 hr in high-glucose DMEM with 10% FBS. Knockdown efficiency was determined by western blot via standard methods. After 3 days of treatment with the various siRNAs, all showed pan-nucleoplasmic foci of γH2AX, and only siRPA1 also caused global foci of γH2AX, but this was evident in only a minor fraction of cells (<20%) even after ~50% knockdown.

For establishment of an inducible GATA4-v5 line, U2OS Ctrl_clone-1 cells were plated onto 24-well plates and cultured for 24 hr. On the following day, cells were incubated with 100 μL (≥2.5 × 10^5 infectious units) rtTA lentivirus and 100 μL (≥2.5 × 10^5 infectious units) tetO-GATA4-V5 lentivirus (provided with methods by the Dr. John D. Gearhart, University of Pennsylvania), 8 μg/mL polybrene (Milipore), and 200 μL full culture media for 2 days. After viral transduction, the cells were re-plated, and on the next day GATA4-v5 expression was induced by culturing of the cells in 2 μg/mL doxycycline for at least 5 days. For de-polymerization of the MT, TW17_clone-2 cells were treated with 100 ng/mL nocodazole (Sigma) for 12 hr.

FISH

U2OS cells and MSCs were fixed by methanol and mounted onto glass slides, and chromosome 1 was labeled with an orange whole-chromosome painting

probe (Creative Bioarray); its centromere was simultaneously labeled with a green VividFISH chromosome enumeration probe (GeneCopoeia). Cell fixation, slide preparation, and probe hybridization were performed according to the manufacturers' protocols. After hybridization, the slides were mounted with AntiFade-DAPI (GeneCopoeia). The labeled, DAPI-stained cells were then imaged using a 150×/1.5 NA oil-immersion objective.

SUPPLEMENTAL INFORMATION

Supplemental Information includes five figures and six tables and can be found with this article online at http://dx.doi.org/10.1016/j.cub.2016.11.049.

AUTHOR CONTRIBUTIONS

J.I., Y.X, C.R.P., and A.A. designed and performed experiments. J.J., C.A., and M.T. performed experiments. S.M.H., R.R.B., A.L., R.A.G., and D.E.D. analyzed results. J.I. and D.E.D. wrote the manuscript.

ACKNOWLEDGMENTS

The authors thank John D. Gearhart (University of Pennsylvania) for the tetO-GATA4-v5 lentiviral system. The authors in this study were supported by the National Cancer Institute of the NIH under PSOC award number U54 CA193417. The content is solely the responsibility of the authors and does not necessarily represent the official views of the NIH.

Received: October 9, 2016
Revised: November 11, 2016
Accepted: November 23, 2016
Published: December 15, 2016

REFERENCES

1. Chamberlain, J.K., and Lichtman, M.A. (1978). Marrow cell egress: specificity of the site of penetration into the sinus. Blood *52*, 959–968.
2. Harada, T., Swift, J., Irianto, J., Shin, J.W., Spinler, K.R., Athirasala, A., Diegmiller, R., Dingal, P.C., Ivanovska, I.L., and Discher, D.E. (2014). Nuclear lamin stiffness is a barrier to 3D migration, but softness can limit survival. J. Cell Biol. *204*, 669–682.
3. Raab, M., Gentili, M., de Belly, H., Thiam, H.R., Vargas, P., Jimenez, A.J., Lautenschlaeger, F., Voituriez, R., Lennon-Duménil, A.M., Manel, N., and Piel, M. (2016). ESCRT III repairs nuclear envelope ruptures during cell migration to limit DNA damage and cell death. Science *352*, 359–362.
4. Irianto, J., Pfeifer, C.R., Xia, Y., Athirasala, A., Ivanovska, I.L., Greenberg, R.E., and Discher, D.E. (2015). Constricted cell migration causes nuclear lamina damage, DNA breaks, and squeeze-out of repair factors. bioRxiv. http://dx.doi.org/10.1101/035626.
5. Ogawa, H., Inouye, S., Tsuji, F.I., Yasuda, K., and Umesono, K. (1995). Localization, trafficking, and temperature-dependence of the Aequorea green fluorescent protein in cultured vertebrate cells. Proc. Natl. Acad. Sci. USA *92*, 11899–11903.
6. Gonzalo, S. (2014). DNA damage and lamins. Adv. Exp. Med. Biol. *773*, 377–399.
7. Denais, C.M., Gilbert, R.M., Isermann, P., McGregor, A.L., te Lindert, M., Weigelin, B., Davidson, P.M., Friedl, P., Wolf, K., and Lammerding, J. (2016). Nuclear envelope rupture and repair during cancer cell migration. Science *352*, 353–358.
8. Macůrek, L., Lindqvist, A., Voets, O., Kool, J., Vos, H.R., and Medema, R.H. (2010). Wip1 phosphatase is associated with chromatin and dephosphorylates gammaH2AX to promote checkpoint inhibition. Oncogene *29*, 2281–2291.
9. Harding, S.M., and Bristow, R.G. (2012). Discordance between phosphorylation and recruitment of 53BP1 in response to DNA double-strand breaks. Cell Cycle *11*, 1432–1444.
10. Alagoz, M., Katsuki, Y., Ogiwara, H., Ogi, T., Shibata, A., Kakarougkas, A., and Jeggo, P. (2015). SETDB1, HP1 and SUV39 promote repositioning of 53BP1 to extend resection during homologous recombination in G2 cells. Nucleic Acids Res. *43*, 7931–7944.
11. Guo, C., Nakazawa, Y., Woodbine, L., Björkman, A., Shimada, M., Fawcett, H., Jia, N., Ohyama, K., Li, T.S., Nagayama, Y., et al. (2015). XRCC4 deficiency in human subjects causes a marked neurological phenotype but no overt immunodeficiency. J. Allergy Clin. Immunol. *136*, 1007–1017.
12. Shanbhag, N.M., Rafalska-Metcalf, I.U., Balane-Bolivar, C., Janicki, S.M., and Greenberg, R.A. (2010). ATM-dependent chromatin changes silence transcription in cis to DNA double-strand breaks. Cell *141*, 970–981.
13. Chen, X., Bahrami, A., Pappo, A., Easton, J., Dalton, J., Hedlund, E., Ellison, D., Shurtleff, S., Wu, G., Wei, L., et al.; St. Jude Children's Research Hospital–Washington University Pediatric Cancer Genome Project (2014). Recurrent somatic structural variations contribute to tumorigenesis in pediatric osteosarcoma. Cell Rep. *7*, 104–112.
14. Irianto, J., Pfeifer, C.R., Xia, Y., and Discher, D.E. (2016). SnapShot: mechanosensing matrix. Cell *165*, 1820–1820.e1.
15. Kovac, M., Blattmann, C., Ribi, S., Smida, J., Mueller, N.S., Engert, F., Castro-Giner, F., Weischenfeldt, J., Kovacova, M., Krieg, A., et al. (2015). Exome sequencing of osteosarcoma reveals mutation signatures reminiscent of BRCA deficiency. Nat. Commun. *6*, 8940.
16. Swift, J., Ivanovska, I.L., Buxboim, A., Harada, T., Dingal, P.C., Pinter, J., Pajerowski, J.D., Spinler, K.R., Shin, J.W., Tewari, M., et al. (2013). Nuclear lamin-A scales with tissue stiffness and enhances matrix-directed differentiation. Science *341*, 1240104.
17. Olive, P.L., Banáth, J.P., and Durand, R.E. (1990). Detection of etoposide resistance by measuring DNA damage in individual Chinese hamster cells. J. Natl. Cancer Inst. *82*, 779–783.
18. Hatch, E.M., Fischer, A.H., Deerinck, T.J., and Hetzer, M.W. (2013). Catastrophic nuclear envelope collapse in cancer cell micronuclei. Cell *154*, 47–60.
19. Wu, J., Lu, L.Y., and Yu, X. (2010). The role of BRCA1 in DNA damage response. Protein Cell *1*, 117–123.
20. Nussenzweig, A., Sokol, K., Burgman, P., Li, L., and Li, G.C. (1997). Hypersensitivity of Ku80-deficient cell lines and mice to DNA damage: the effects of ionizing radiation on growth, survival, and development. Proc. Natl. Acad. Sci. USA *94*, 13588–13593.
21. Irianto, J., Pfeifer, C.R., Bennett, R.R., Xia, Y., Ivanovska, I.L., Liu, A.J., Greenberg, R.A., and Discher, D.E. (2016). Nuclear constriction segregates mobile nuclear proteins away from chromatin. Mol. Biol. Cell. Published online October 26, 2016. http://dx.doi.org/10.1091/mbc.E16-06-0428.
22. Difilippantonio, M.J., Zhu, J., Chen, H.T., Meffre, E., Nussenzweig, M.C., Max, E.E., Ried, T., and Nussenzweig, A. (2000). DNA repair protein Ku80 suppresses chromosomal aberrations and malignant transformation. Nature *404*, 510–514.
23. Holstege, H., van Beers, E., Velds, A., Liu, X., Joosse, S.A., Klarenbeek, S., Schut, E., Kerkhoven, R., Klijn, C.N., Wessels, L.F., et al. (2010). Cross-species comparison of aCGH data from mouse and human BRCA1- and BRCA2-mutated breast cancers. BMC Cancer *10*, 455.
24. Wang, Y., Putnam, C.D., Kane, M.F., Zhang, W., Edelmann, L., Russell, R., Carrión, D.V., Chin, L., Kucherlapati, R., Kolodner, R.D., and Edelmann, W. (2005). Mutation in Rpa1 results in defective DNA double-strand break repair, chromosomal instability and cancer in mice. Nat. Genet. *37*, 750–755.
25. Dudgeon, C., Chan, C., Kang, W., Sun, Y., Emerson, R., Robins, H., and Levine, A.J. (2014). The evolution of thymic lymphomas in p53 knockout mice. Genes Dev. *28*, 2613–2620.
26. Barlow, C., Hirotsune, S., Paylor, R., Liyanage, M., Eckhaus, M., Collins, F., Shiloh, Y., Crawley, J.N., Ried, T., Tagle, D., and Wynshaw-Boris, A. (1996). Atm-deficient mice: a paradigm of ataxia telangiectasia. Cell *86*, 159–171.
27. Dingal, P.C., Bradshaw, A.M., Cho, S., Raab, M., Buxboim, A., Swift, J., and Discher, D.E. (2015). Fractal heterogeneity in minimal matrix models

of scars modulates stiff-niche stem-cell responses via nuclear exit of a mechanorepressor. Nat. Mater. *14*, 951–960.

28. Hass, C.S., Gakhar, L., and Wold, M.S. (2010). Functional characterization of a cancer causing mutation in human replication protein A. Mol. Cancer Res. *8*, 1017–1026.
29. Jeon, G.S., Kim, K.Y., Hwang, Y.J., Jung, M.K., An, S., Ouchi, M., Ouchi, T., Kowall, N., Lee, J., and Ryu, H. (2012). Deregulation of BRCA1 leads to impaired spatiotemporal dynamics of γ-H2AX and DNA damage responses in Huntington's disease. Mol. Neurobiol. *45*, 550–563.
30. Jensen, R.B., Ozes, A., Kim, T., Estep, A., and Kowalczykowski, S.C. (2013). BRCA2 is epistatic to the RAD51 paralogs in response to DNA damage. DNA Repair (Amst.) *12*, 306–311.
31. Vandersickel, V., Depuydt, J., Van Bockstaele, B., Perletti, G., Philippe, J., Thierens, H., and Vral, A. (2010). Early increase of radiation-induced γH2AX foci in a human Ku70/80 knockdown cell line characterized by an enhanced radiosensitivity. J. Radiat. Res. (Tokyo) *51*, 633–641.
32. Fiszer-Kierzkowska, A., Vydra, N., Wysocka-Wycisk, A., Kronekova, Z., Jarząb, M., Lisowska, K.M., and Krawczyk, Z. (2011). Liposome-based DNA carriers may induce cellular stress response and change gene expression pattern in transfected cells. BMC Mol. Biol. *12*, 27.
33. Chen, W.T., Ebelt, N.D., Stracker, T.H., Xhemalce, B., Van Den Berg, C.L., and Miller, K.M. (2015). ATM regulation of IL-8 links oxidative stress to cancer cell migration and invasion. eLife *4*, e07270.
34. Carter, N.P. (2007). Methods and strategies for analyzing copy number variation using DNA microarrays. Nat. Genet. *39* (7, Suppl), S16–S21.
35. Qiu, Z., Zou, K., Zhuang, L., Qin, J., Li, H., Li, C., Zhang, Z., Chen, X., Cen, J., Meng, Z., et al. (2016). Hepatocellular carcinoma cell lines retain the genomic and transcriptomic landscapes of primary human cancers. Sci. Rep. *6*, 27411.
36. Thiagalingam, S., Laken, S., Willson, J.K., Markowitz, S.D., Kinzler, K.W., Vogelstein, B., and Lengauer, C. (2001). Mechanisms underlying losses of heterozygosity in human colorectal cancers. Proc. Natl. Acad. Sci. USA *98*, 2698–2702.
37. Sankaranarayanan, P., Schomay, T.E., Aiello, K.A., and Alter, O. (2015). Tensor GSVD of patient- and platform-matched tumor and normal DNA copy-number profiles uncovers chromosome arm-wide patterns of tumor-exclusive platform-consistent alterations encoding for cell transformation and predicting ovarian cancer survival. PLoS ONE *10*, e0121396.
38. Jaenisch, R., and Bird, A. (2003). Epigenetic regulation of gene expression: how the genome integrates intrinsic and environmental signals. Nat. Genet. *33* (*Suppl*), 245–254.
39. Huang, W., Sherman, B.T., and Lempicki, R.A. (2009). Systematic and integrative analysis of large gene lists using DAVID bioinformatics resources. Nat. Protoc. *4*, 44–57.
40. Tilney, L.G., and Gibbins, J.R. (1969). Microtubules in the formation and development of the primary mesenchyme in Arbacia punctulata. II. An experimental analysis of their role in development and maintenance of cell shape. J. Cell Biol. *41*, 227–250.
41. Rivera-Feliciano, J., Lee, K.H., Kong, S.W., Rajagopal, S., Ma, Q., Springer, Z., Izumo, S., Tabin, C.J., and Pu, W.T. (2006). Development of heart valves requires Gata4 expression in endothelial-derived cells. Development *133*, 3607–3618.
42. Güemes, M., Garcia, A.J., Rigueur, D., Runke, S., Wang, W., Zhao, G., Mayorga, V.H., Atti, E., Tetradis, S., Péault, B., et al. (2014). GATA4 is essential for bone mineralization via ERα and TGFβ/BMP pathways. J. Bone Miner. Res. *29*, 2676–2687.
43. Engler, A.J., Sen, S., Sweeney, H.L., and Discher, D.E. (2006). Matrix elasticity directs stem cell lineage specification. Cell *126*, 677–689.
44. Song, I., Kim, K., Kim, J.H., Lee, Y.K., Jung, H.J., Byun, H.O., Yoon, G., and Kim, N. (2014). GATA4 negatively regulates osteoblast differentiation by downregulation of Runx2. BMB Rep. *47*, 463–468.
45. Irianto, J., Xia, Y., Pfeifer, C.R., Greenberg, R.A., and Discher, D.E. (2016). As a nucleus enters a small pore, chromatin stretches and maintains integrity even with DNA breaks. Biophys. J. Published online October 27, 2016. http://dx.doi.org/10.1016/j.bpj.2016.09.047.
46. Maciejowski, J., Li, Y., Bosco, N., Campbell, P.J., and de Lange, T. (2015). Chromothripsis and kataegis induced by telomere crisis. Cell *163*, 1641–1654.
47. De Vos, W.H., Houben, F., Kamps, M., Malhas, A., Verheyen, F., Cox, J., Manders, E.M., Verstraeten, V.L., van Steensel, M.A., Marcelis, C.L., et al. (2011). Repetitive disruptions of the nuclear envelope invoke temporary loss of cellular compartmentalization in laminopathies. Hum. Mol. Genet. *20*, 4175–4186.
48. Tamiello, C., Kamps, M.A., van den Wijngaard, A., Verstraeten, V.L., Baaijens, F.P., Broers, J.L., and Bouten, C.C. (2013). Soft substrates normalize nuclear morphology and prevent nuclear rupture in fibroblasts from a laminopathy patient with compound heterozygous LMNA mutations. Nucleus *4*, 61–73.
49. Nuciforo, P.G., Luise, C., Capra, M., Pelosi, G., and d'Adda di Fagagna, F. (2007). Complex engagement of DNA damage response pathways in human cancer and in lung tumor progression. Carcinogenesis *28*, 2082–2088.
50. Gerlinger, M., Rowan, A.J., Horswell, S., Larkin, J., Endesfelder, D., Gronroos, E., Martinez, P., Matthews, N., Stewart, A., Tarpey, P., et al. (2012). Intratumor heterogeneity and branched evolution revealed by multiregion sequencing. N. Engl. J. Med. *366*, 883–892.

Current Biology, Volume *27*

Supplemental Information

DNA Damage Follows Repair Factor Depletion and Portends Genome Variation in Cancer Cells after Pore Migration

Jerome Irianto, Yuntao Xia, Charlotte R. Pfeifer, Avathamsa Athirasala, Jiazheng Ji, Cory Alvey, Manu Tewari, Rachel R. Bennett, Shane M. Harding, Andrea J. Liu, Roger A. Greenberg, and Dennis E. Discher

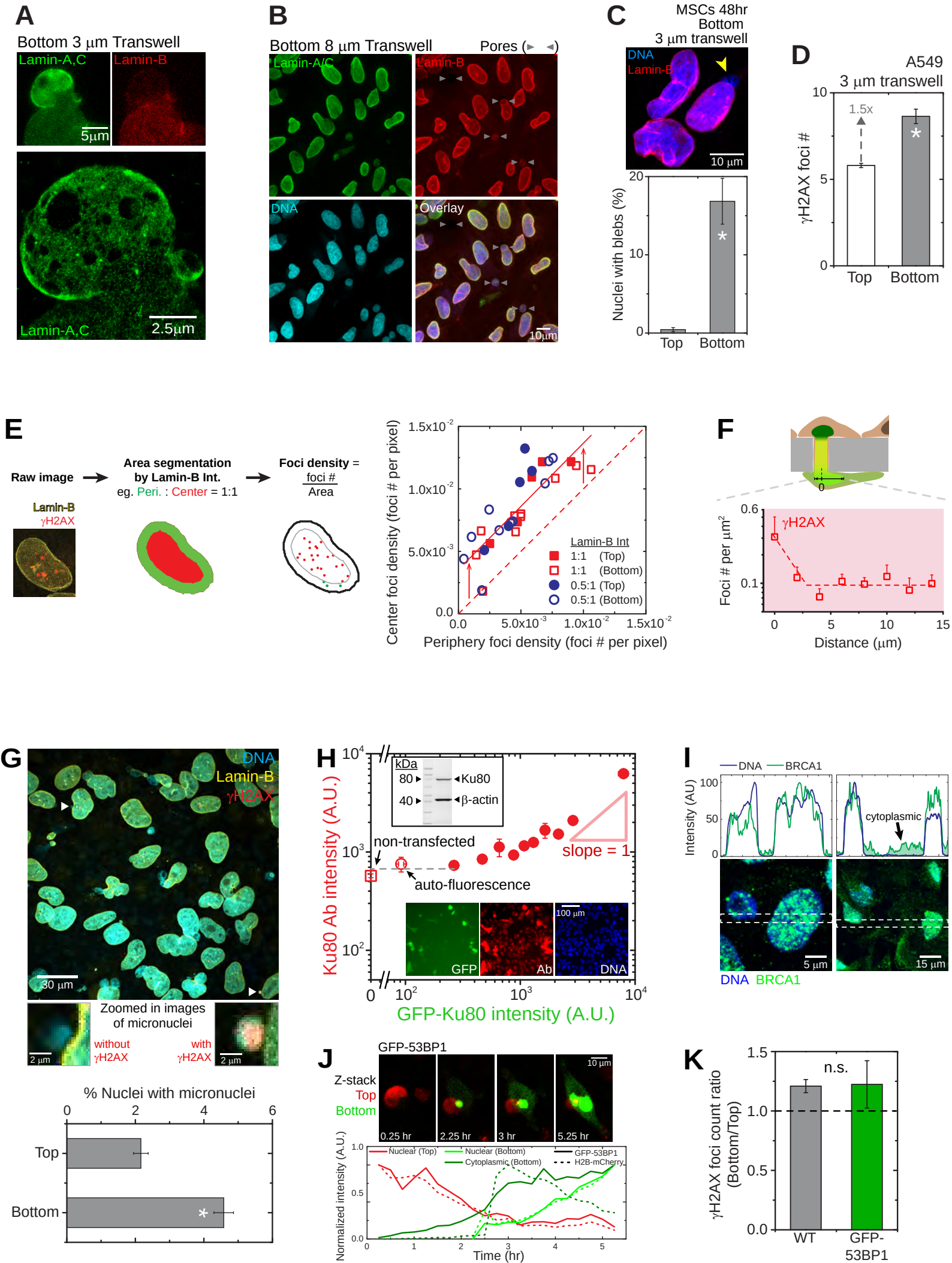
A
Bottom 3 μm Transwell
Lamin-A,C
Lamin-B
5μm
Lamin-A,C
2.5μm
B
Bottom 8 μm Transwell
Pores (► ◄)
Lamin-A/C
Lamin-B
DNA
Overlay
10μm
C
MSCs 48hr
Bottom
3 μm transwell
DNA
Lamin-B
10 μm
Nuclei with blebs (%)
Top
Bottom
D
A549
3 μm transwell
γH2AX foci #
1.5x
Top
Bottom
E
Raw image
Area segmentation
by Lamin-B Int.
eg. Peri. : Center = 1:1
Foci density =
foci #
Area
Lamin-B
γH2AX
Center foci density (foci # per pixel)
Periphery foci density (foci # per pixel)
Lamin-B Int
1:1 (Top)
1:1 (Bottom)
0.5:1 (Top)
0.5:1 (Bottom)
F
γH2AX
Foci # per μm²
Distance (μm)
G
DNA
Lamin-B
γH2AX
30 μm
Zoomed in images
of micronuclei
without
γH2AX
with
γH2AX
2 μm
% Nuclei with micronuclei
Top
Bottom
H
kDa
80
40
Ku80
β-actin
non-transfected
slope = 1
auto-fluorescence
GFP
Ab
DNA
100 μm
Ku80 Ab intensity (A.U.)
GFP-Ku80 intensity (A.U.)
I
DNA
BRCA1
Intensity (AU)
cytoplasmic
5 μm
15 μm
DNA BRCA1
J
GFP-53BP1
Z-stack
Top
Bottom
10 μm
0.25 hr
2.25 hr
3 hr
5.25 hr
Nuclear (Top)
Nuclear (Bottom)
Cytoplasmic (Bottom)
GFP-53BP1
H2B-mCherry
Normalized intensity (A.U.)
Time (hr)
K
γH2AX foci count ratio
(Bottom/Top)
n.s.
WT
GFP-
53BP1

Figure S1. Constricted migration also increases nuclear blebs in MSCs and DNA damage in A549 cells. DNA damage sites observed tend to be at the center of the nucleus, micronuclei number are slightly increased and BRCA1 mis-localize to cytoplasm. Overexpressed GFP-53BP1 also mis-localize to cytoplasm and does not rescue DNA damage post migration. Migration through larger pores does not perturb nuclear morphology. Related to Fig.1 and Fig.2. (A) Super resolution imaging of a nuclear bleb after constricted migration reveals a dilated meshwork of Lamin-A,C**. (B)** Cells that have migrated through large 8 μm pores do not exhibit major nuclear damage. **(C)** Migration of hMSCs through 3 μm pores leads to an increase in nuclear blebs positive nuclei, which is absent of lamin-B (≥100 nuclei per conditions, $*p < 0.05$). **(D)** Migration of A549, human lung carcinoma cell line, through 3μm pores also leads to an increase in γH2AX foci count (≥100 nuclei per conditions, n ≥ 3 expts, $*p < 0.05$). **(E)** Nuclear area was segmented to periphery and center by lamin-B integrated intensity. γH2AX foci count reveals that foci tend to be located at the center of the nucleus (n = 15 nuclei). **(F)** DNA damage foci are evident near the pore at bottom and are relatively homogeneous elsewhere (n = 14 nuclei). **(G)** Although higher number of micronuclei were found after 3 μm pore migration, it is relatively rare compared to the pre-dominant nuclear blebs (≥ 3 transwells, n ≥ 3 expts, $*p < 0.05$). Some of the micronuclei stained for γH2AX, indicative of DNA damage (white arrows). **(H)** Specificity of Ku80 antibody was validated by immuno-staining U2OS cells with GFP-Ku80 over-expression. At lower GFP intensity level, Ku80 antibody intensity is statistically the same as the non-transfected cells (dashed line). At higher over-expression level, Ku80 antibody intensity increases proportionally to GFP intensity (≥ 1600 cells). (Inset) Immunoblot of Ku80 and β-actin shows clear bands only at the corresponding molecular weight, again suggesting specificity of the antibodies. **(I)** Representative images and intensity profiles showing increased BRCA1 mis-localization to the cytoplasm (green shaded) after migration through 3 μm pores at the bottom of the transwell. **(J)** Live imaging of GFP- 53BP1 and H2B-mCherry-overexpressing U2OS cells reveals nuclear rupture —with leakage of GFP/m-Cherry into the cytoplasm. H2B-mCherry signal re-localized rapidly into the nucleus (<3 hours)[S1]. **(K)** Over-expression of GFP- 53BP1 in U2OS cells does not rescue the migration-induced DNA damage, as shown by the γH2AX foci ratio (≥ 100 cells per conditions, n ≥ 2 expts). Error bars: Avg.±S.E.M.

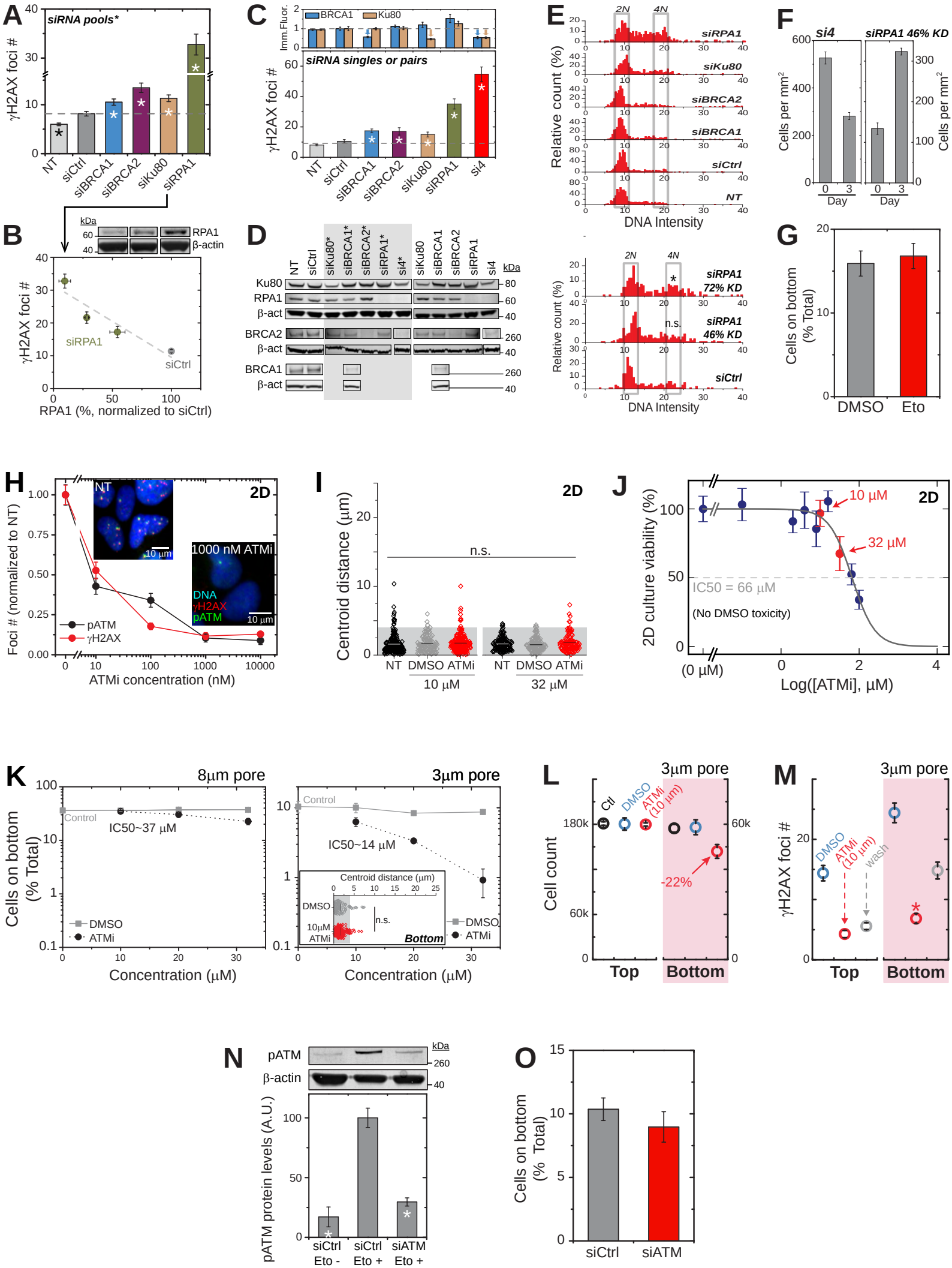
A
siRNA pools*
γH2AX foci #
NT
siCtrl
siBRCA1
siBRCA2
siKu80
siRPA1
B
kDa
RPA1
β-actin
γH2AX foci #
siRPA1
siCtrl
RPA1 (%, normalized to siCtrl)
C
Imm.Fluor.
BRCA1
Ku80
siRNA singles or pairs
γH2AX foci #
si4
D
Ku80
RPA1
β-act
BRCA2
BRCA1
E
2N
4N
siRPA1
siKu80
siBRCA2
siBRCA1
siCtrl
NT
Relative count (%)
DNA Intensity
siRPA1 72% KD
siRPA1 46% KD
n.s.
F
si4
siRPA1 46% KD
Cells per mm²
Day
G
Cells on bottom (% Total)
DMSO
Eto
H
2D
NT
1000 nM ATMi
DNA
γH2AX
pATM
Foci # (normalized to NT)
ATMi concentration (nM)
I
2D
Centroid distance (μm)
n.s.
NT
DMSO
ATMi
10 μM
32 μM
J
2D
10 μM
32 μM
IC50 = 66 μM
(No DMSO toxicity)
2D culture viability (%)
(0 μM)
Log([ATMi], μM)
K
8μm pore
3μm pore
Control
IC50~37 μM
IC50~14 μM
DMSO
ATMi
Cells on bottom (% Total)
Concentration (μM)
Centroid distance (μm)
Bottom
L
3μm pore
Ctl
DMSO
ATMi (10 μm)
-22%
Cell count
Top
Bottom
M
3μm pore
DMSO
ATMi (10 μm)
wash
γH2AX foci #
Top
Bottom
N
pATM
β-actin
kDa
pATM protein levels (A.U.)
siCtrl Eto -
siCtrl Eto +
siATM Eto +
O
Cells on bottom (% Total)
siCtrl
siATM

Figure S2. ATMi kills cell on 2D culture at high dosage and after migration with lower dosage. Etoposide-induced DNA damage does not impede migration. Knockdown of some DNA repair factors are titratable and lead to accumulation of DNA damage, increase of DNA content and some cell death. Related to Figure 3. (A) Treating U2OS with single siRNA pool of BRCA1, BRCA2, RPA1 and Ku80 leads to increased γH2AX foci count. However, the most significant effect was observed in the siRPA1 group (≥ 150 nuclei per conditions, $*p < 0.05$ compared to siCtrl). **(B)** Depletion of siRPA1 is titratable by using less siRNAs, the levels of knockdown are reflected by the γH2AX foci count, majority of the nuclei have distinctive γH2AX foci, while minority of nuclei have "global" γH2AX staining, where the whole nucleoplasmic region is positive for γH2AX (≥ 150 nuclei per conditions, n ≥ 3 expts, $*p < 0.05$ compared to siCtrl). **(C)** In order to validate siRNAs specificity, another set of siRNAs with different sequences was purchased from a different source (see Methods). Most of the siRNAs comprise of a single sequence, except for siKu80 that contains a pair of siRNA sequences. Specificity of the knockdown was illustrated by the upper plot, where BRCA1 and Ku80 depletion was only observed in siBRCA1 and siKu80 samples, respectively, in addition to the si4 sample. Indeed, the increase of γH2AX foci count was also observed with these siRNAs (≥ 150 nuclei per conditions, n = 2 expts, $*p < 0.05$ compared to siCtrl). **(D)** Specificity of the DNA repair factors depletion by siRNA treatments was confirmed by immuno-blots (* for the siRNA singles and pairs used in Figure S2C). **(E)** Treating U2OS with single siRNA pools also leads to increased DNA content (≥ 150 nuclei per conditions, n ≥ 3 expts, $*p < 0.05$ compared to siCtrl, statistical comparison between distributions were done with KS test). **(F)** si4 treatment induces cell death within the 3 days of culture after treatment, but knockdown of RPA1 by 46% allows for cell growth (n ≥ 3 expts). **(G)** Exposing the cells to 10 μM Etoposide does not impede the migration, even with the induced DNA damage (Figure 1H, n = 3 transwell membranes). **(H, I)** Inhibition efficiency of ATMi was measured by foci counts for γH2AX and phosphorylated ATM (pATM). Both γH2AX and pATM foci can be seen in non-treated cells per representative image. Foci counts decreased ~50% at 10 nM and plateau at 0.1 to 1 μM (≥ 150 nuclei per condition, n ≥ 3 expts). Comet assay did not show accumulation of DNA damage after ATMi treatment, even at very high drug 32 μM concentrations (≥ 200 nuclei per group, n = 3 expts). **(J)** Colorimetric toxicity assay of ATMi treatment on U2OS 2D culture shows an IC50 of 66 μM (n = 3 expts). **(K)** The percentage of cells that migrated through the transwell in 24 hours is higher for 8 μm pores than for 3 μm pores, and is reduced only for very high doses of ATMi (10, 20 and 32 μM), with 50% fewer cells (IC50) of 37 and 14 μM for 8 μm and 3 μm pores, respectively. DMSO solvent control does not affect the migration ratios (≥ 3 transwell each condition, n ≥ 3 expts). The inset shows 10 μM ATMi during migration also does not cause more comet-detected DNA damage when compared to the corresponding DMSO group (≥ 200 nuclei each condition, n ≥ 3 expts). **(L, M)** Inhibition with ATMi (10 μM) of ATM kinase which phosphorylates H2AX (to make γH2AX) during the 24 hrs of constricted migration decreases cell numbers on the Bottom but not the Top. The result is consistent with past evidence of migration-dependent cell death. For both Top and Bottom, ATMi strongly decreases γH2AX, but more foci on Bottom are resistant (≥ 45 nuclei per condition, n ≥ 3 expts, $*p < 0.05$). **(N)** siATM treatment leads to a decrease of pATM in samples exposed to 10 μM etoposide (n = 3 western blots, $*p < 0.05$ compared to siCtrl treated with etoposide). **(O)** siATM does not inhibit migration (n = 3 transwell membranes). Error bars: Avg.±S.E.M.

A

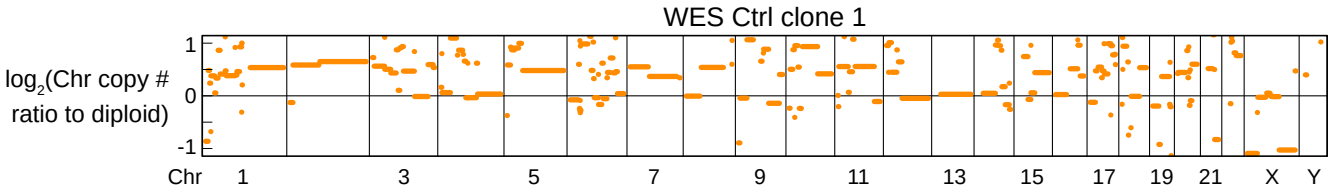

B

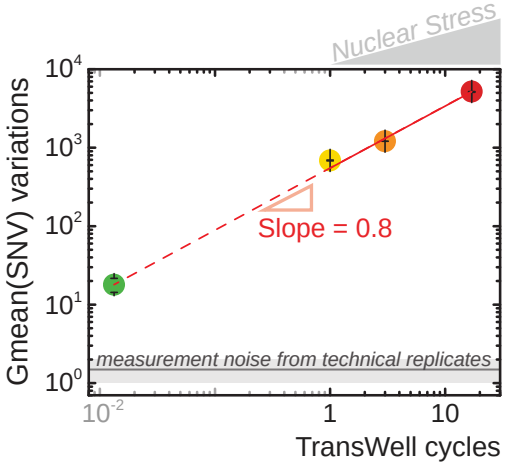

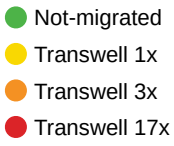

C

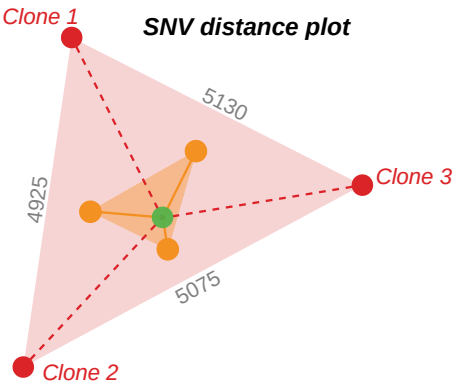

D

	Control Clone1	Control Clone2	Control Clone3	Control Clone4	Control Clone5	Control Clone6	TW3 Clone1	TW3 Clone2	TW3 Clone3	TW17 Clone1	TW17 Clone2	TW17 Clone3
Control-Clone1	0	36	0	32	13	2	1043	394	866	2455	2508	2626
Control-Clone2	36	0	36	32	13	4	1079	430	902	2491	2544	2662
Control-Clone3	0	36	0	32	13	2	1043	394	866	2455	2508	2626
Control-Clone4	32	32	32	0	21	34	1075	426	898	2455	2529	2660
Control-Clone5	13	13	13	21	0	15	1056	407	879	2476	2508	2641
Control-Clone6	2	4	2	34	15	0	1045	398	868	2489	2523	2626
TW3-Clone1	1043	1079	1043	1075	1056	1045	0	1433	1907	3494	3547	3665
TW3-Clone2	394	430	394	426	407	398	1433	0	1258	2845	2592	3016
TW3-Clone3	866	902	866	898	879	868	1907	1258	0	3319	1746	3462
*TW17-Clone1	2455	2491	2455	2455	2476	2489	3494	2845	3319	0	4925	5075
*TW17-Clone2	2508	2544	2508	2529	2508	2523	3547	2592	1746	4925	0	5130
*TW17-Clone3	2626	2662	2626	2660	2641	2626	3665	3016	3462	5075	5130	0

E

Expt 1	Clone 1	Clone 2	Clone 3	Clone 4	Clone 5	Clone 6
Pre-migration clone (Gain)	0	0	24	38	53	72
Pre-migration clone (Loss)	0	0	1	0	1	2
Pre-migration clone (Total)	0	0	25	38	54	74
Clone 1	0	0	25	38	55	74
Clone 2	0	0	25	38	55	74
Clone 3	25	25	0	63	80	75
Clone 4	38	38	63	0	93	154
Clone 5	55	55	80	93	0	128
Clone 6	74	74	75	154	128	0

F

Expt 2	TW3 clone 1	TW3 clone 2	TW3 clone 3
Ctrl clone 1 (Gain)	15	27	15
Ctrl clone 1 (Loss)	4	0	5
Ctrl clone 1 (Total)	19	27	20
TW3 clone 1	0	49	49
TW3 clone 2	49	0	58
TW3 clone 3	49	58	0

G

Expt 3	3 µm clone 1	3 µm clone 2	3 µm clone 3	3 µm clone 4
Ctrl clone 1 (Gain)	0	6	10	28
Ctrl clone 1 (Loss)	0	0	0	0
Ctrl clone 1 (Total)	0	6	10	28
3 µm clone 1	0	7	21	30
3 µm clone 2	7	0	10	37
3 µm clone 3	21	10	0	35
3 µm clone 4	30	37	35	0

	8 µm clone 1	8 µm clone 2	8 µm clone 3	8 µm clone 4	8 µm clone 5	8 µm clone 6
Ctrl clone 1 (Gain)	0	0	0	0	8	17
Ctrl clone 1 (Loss)	0	0	0	0	0	0
Ctrl clone 1 (Total)	0	0	0	0	8	17
8 µm clone 1	0	0	0	0	8	20
8 µm clone 2	0	0	0	0	9	17
8 µm clone 3	0	0	0	0	9	19
8 µm clone 4	0	0	0	0	10	17
8 µm clone 5	8	9	9	10	0	27
8 µm clone 6	20	17	19	17	27	0

Figure S3. Chromosome copy number derived from whole exome sequencing (WES) data agrees with data of aCGH. Number of SNVs increase with migration, increasing the heterogeneity of the cell population. Variations in ΔLOH is smallest for clones migrated through 8 μm transwells. Related to Figure 4 and Figure 5. (A) Chromosome copy number derived from whole exome sequencing (WES) data of control clone 1 agrees with the aCGH data in Figure 4C. Chromosome copy number from control clone 1 WES data was acquired by using CNVkit software package, compared against the computed "flat" diploid reference[S2], then the data were shifted up (by $\log_2(0.3)$) such that the diploid regions of WES and aCGH agree with each other, i.e. chromosome 4q, 12q and 13. CNVkit is best for comparisons of two samples, where data shifting is not required, as done in Figure S4. **(B,C)** Considering the data from Figure 5, instead of comparing to Ctrl clone 1, the three clones of each group are compared to each other. As the cells migrate, SNVs between clones increase. Measurement noise is derived from technical controls from multiple arrays ($n \geq 3$ clones per condition). **(D)** SNV heatmap showing pairwise comparisons of the different SNPa samples. Numbers in the heatmap indicate number of probes detected within the SNV pair comparison. Bulk samples and control clones have relatively low SNVs, indicative of a homogeneous population. Migrations through the 3 μm transwells increase number of SNVs. **(E,F,G)** SNV confirmed changes in LOH's (in Mb, see text or methods) of TW3 clones from experiment 1 (Figure 4E-H), 2 (Figure 5A-D) and 3 are listed as LOH gain, loss and total (gain+loss). Pairwise comparison of the clones are listed below row 3 of each heatmap. Most of the LOH gains are confirmed by SNV calls, but not LOH losses. LOH variations are lowest after 8 μm migration. Error bars: Avg.±S.E.M.

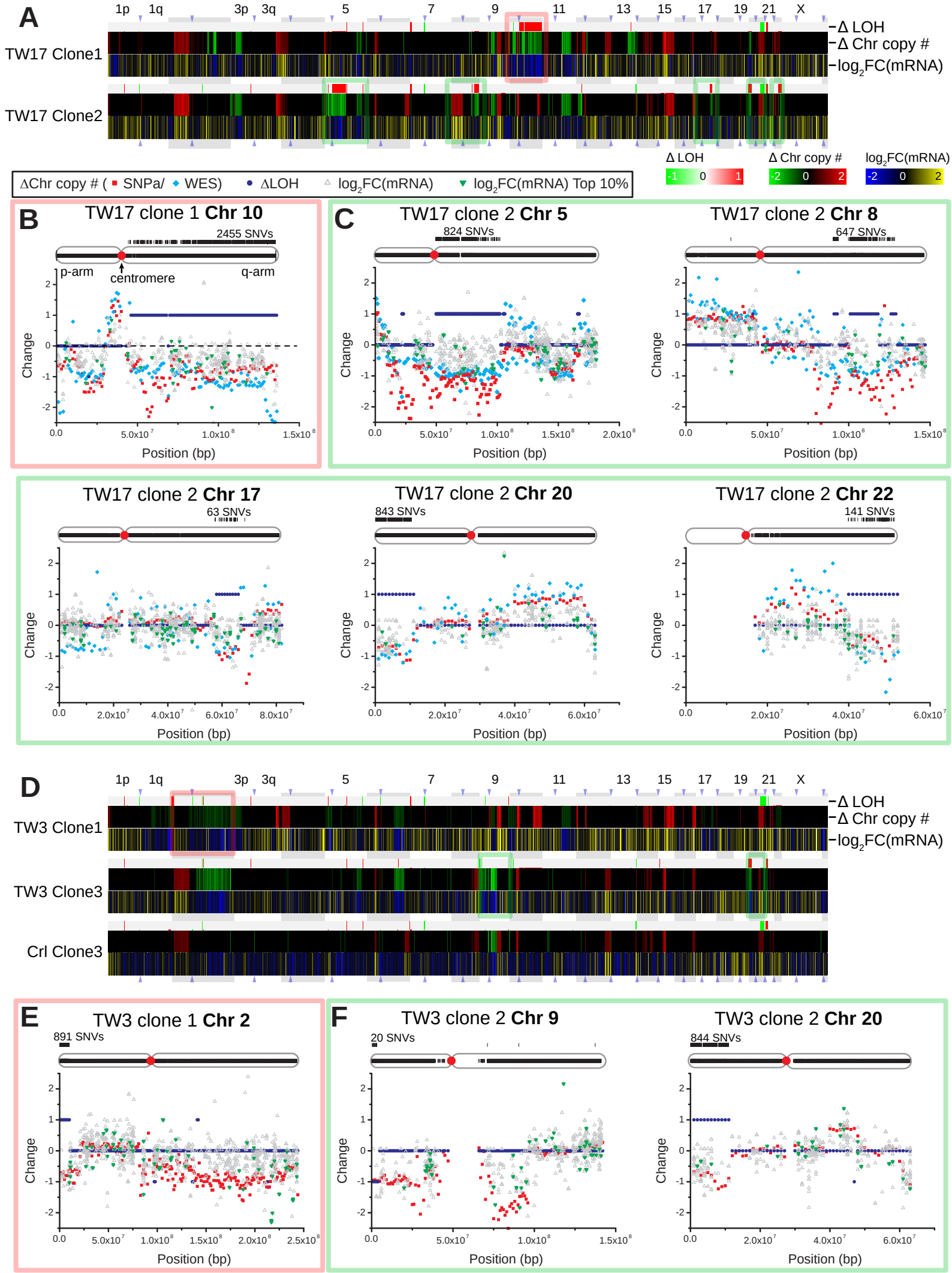
A
1p 1q 3p 3q 5 7 9 11 13 15 17 19 21 X
TW17 Clone1
TW17 Clone2
Δ LOH
Δ Chr copy #
log2FC(mRNA)
ΔChr copy # (SNPa/ WES)
ΔLOH
log2FC(mRNA)
log2FC(mRNA) Top 10%
B
TW17 clone 1 Chr 10
2455 SNVs
p-arm
centromere
q-arm
C
TW17 clone 2 Chr 5
824 SNVs
TW17 clone 2 Chr 8
647 SNVs
TW17 clone 2 Chr 17
63 SNVs
TW17 clone 2 Chr 20
843 SNVs
TW17 clone 2 Chr 22
141 SNVs
Change
Position (bp)
D
TW3 Clone1
TW3 Clone3
Crl Clone3
E
TW3 clone 1 Chr 2
891 SNVs
F
TW3 clone 2 Chr 9
20 SNVs
TW3 clone 2 Chr 20
844 SNVs

Figure S4. mRNA, ΔCN, ΔLOH and SNVs data are consistent with each other, showing partial loss and gain of the chromosomes. Related to Figure 5. (A,D) Change in LOH (ΔLOH), change in chromosome copy number (ΔChr copy #) and log2 of mRNA fold change (log_2FC(mRNA)) heatmaps from the study involved in Figure 5. Although the samples here are subtracted by the data of Control clone 1, differences between samples are still observed and also increase with number of constricted migration, as shown in Figure 5 when samples were subtracted by pre-migration sample. Consistent patterns can be observed between ΔChr copy # and log_2FC(mRNA), when a region gain chromosome copy number (red), it is often accompanied by an increase in mRNA levels (yellow), and vice versa. Compliment of Figure 5G. **(B,C,E,F)** Various chromosomal plots from the heatmaps in Figure S4A, providing a zoomed in plot of a given chromosome for ΔChr copy # from SNP array (SNPa) and whole exome sequencing (WES), ΔLOH, SNVs and mRNA fold change. Black ticks on top of each plot indicate the SNPa probes location for a given chromosome, with reference to the centromere (red circle). SNVs are indicated as an upward shift of the ticks. The more reliable highly abundant transcripts (top 10% expressing mRNAs, green) also follow the ΔChr copy # pattern.

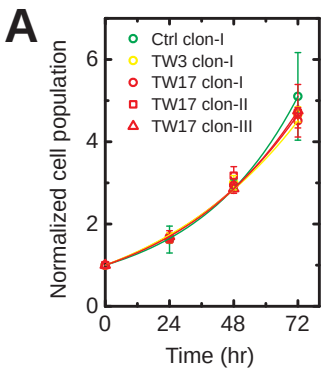
A
Ctrl clon-I
TW3 clon-I
TW17 clon-I
TW17 clon-II
TW17 clon-III
Normalized cell population
Time (hr)

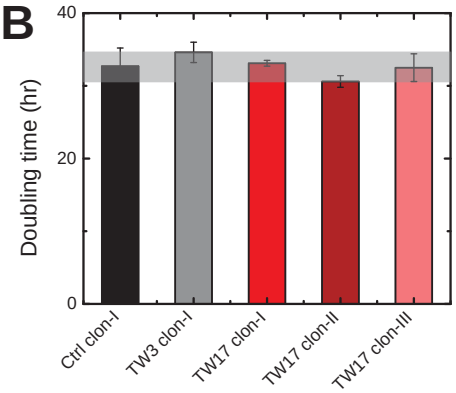
B
Doubling time (hr)
Ctrl clon-I
TW3 clon-I
TW17 clon-I
TW17 clon-II
TW17 clon-III

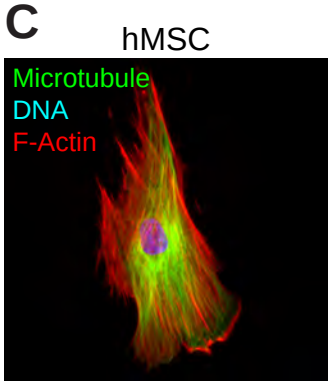
C
hMSC
Microtubule
DNA
F-Actin

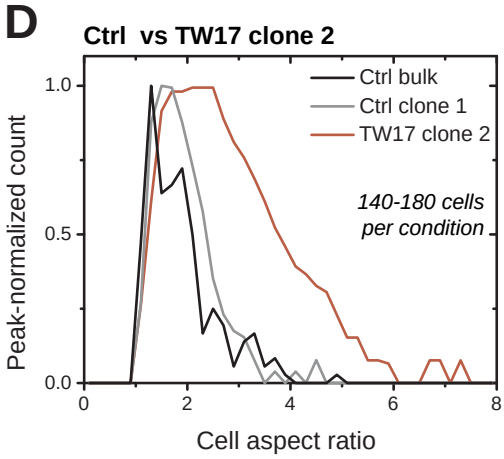
D
Ctrl vs TW17 clone 2
Ctrl bulk
Ctrl clone 1
TW17 clone 2
140-180 cells per condition
Peak-normalized count
Cell aspect ratio

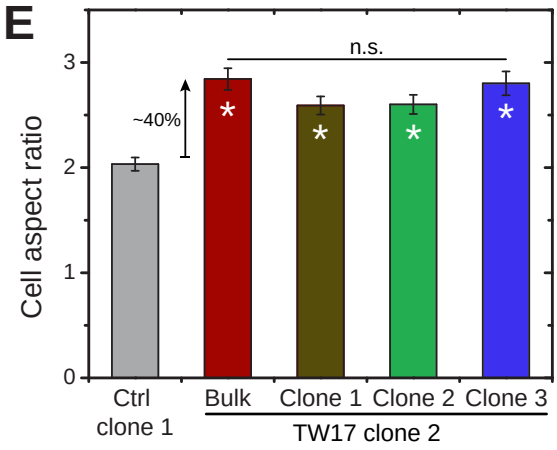
E
Cell aspect ratio
~40%
n.s.
Ctrl clone 1
Bulk
Clone 1
Clone 2
Clone 3
TW17 clone 2

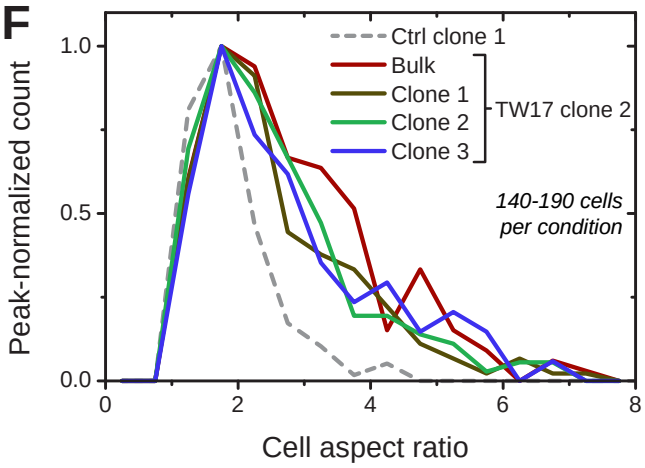
F
Ctrl clone 1
Bulk
Clone 1
Clone 2
Clone 3
TW17 clone 2
140-190 cells per condition
Peak-normalized count
Cell aspect ratio

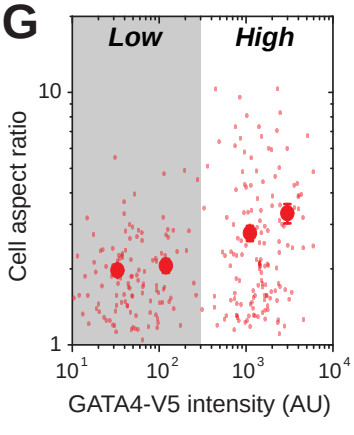
G
Low
High
Cell aspect ratio
GATA4-V5 intensity (AU)

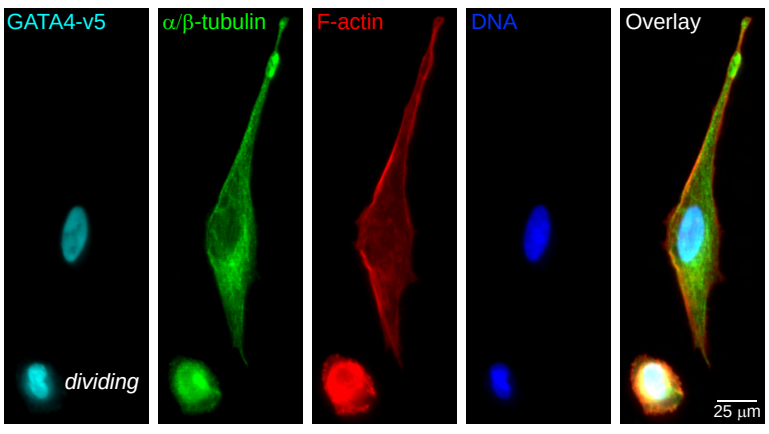
H
GATA4-v5
α/β-tubulin
F-actin
DNA
Overlay
dividing
25 μm

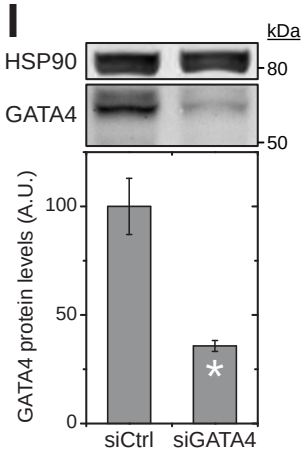
I
kDa
HSP90
GATA4
80
50
GATA4 protein levels (A.U.)
siCtrl
siGATA4

Figure S5. Multiple constricted migration does not alter proliferation rate, but one of the migrated clone has altered cell morphology. The elongated morphology is driven by tubulin organization and GATA4, which can be depleted by siGATA4 treatment. Related to Figure 6. (A,B) Proliferation rate and doubling time stay relatively constant between the non-migrated and migrated clones. **(C)** hMSC showing alignment of microtubule along the length of the cell, giving it an elongated cell morphology. **(D)** Cell aspect ratio distribution of Ctrl bulk, Ctrl clone 1 and TW17 clone 2, showing the shift to an elongated cell morphology for TW17 clone 2 ($\geq$ 140 cells per condition, n $\geq$ 3 expts, $*p < 0.05$). **(E,F)** Single cell clones were isolated from TW17 clone 2 and their cell morphology were quantified from F-actin staining by phalloidin. Both averaged aspect ratio and distribution of the clones are similar to the bulk TW17 clone 2 ($*p < 0.05$ compared to Ctrl clone 1). **(G)** Cell aspect ratio scatter plot of cells expressing GATA4-v5, showing an increase in aspect ratio with higher GATA4-v5 expression. **(H)** Highly spindle U2OS with the overexpression of GATA4-v5 has microtubules along the length of the cell, resemblance of hMSC in (C). **(I)** siGATA4 treatment on TW17 clone 2 cells leads to a decrease in GATA4 protein levels (n = 3 western blots, $*p < 0.05$ compared to siCtrl). Error bars: Avg.±S.E.M.

Table S1. Clonality of U2OS cultures as measured by comparative genome hybridization arrays, aCGH. Related to Figure 4 and 5, with additional information in Table S6.

Culture	% clonality
Control bulk	87.2%
Control clone 1	95.2%
TW3 clone 1	95.5%
TW3 clone 2	100%
TW3 clone 3	98.9%
TW17 clone 1	100%
TW17 clone 2	98.7%
TW17 clone 3	100%

Table S2. Chromosome number estimates were derived from aCGH data for Control bulk and clone 1 sample in Figure 4B-C. Chromosome total length of each chromosome was calculated by adding the chromosome copy number calls of the corresponding chromosome. Chromosome number was estimated by dividing the chromosome total length by the 1 Mb windows of each chromosome, hence it is the average chromosome copy number call.

Control bulk	**Chr**	**Chr number estimate**	**Chr total length (Mb)**
	1	2.98	682.29
	2	3.21	775.70
	3	2.73	534.71
	4	2.51	474.62
	5	3.05	542.07
	6	2.70	455.91
	7	2.61	411.85
	8	3.50	507.17
	9	2.77	340.80
	10	3.24	433.66
	11	2.83	375.79
	12	2.75	362.55
	13	2.06	199.71
	14	2.87	255.64
	15	2.89	240.01
	16	2.88	233.31
	17	3.07	245.94
	18	2.65	203.97
	19	2.51	145.45
	20	3.13	191.01
	21	2.83	102.04
	22	4.29	154.52
	X	1.57	237.75
	TOTAL	**65.62**	**8106.47**

Control clone 1	**Chr**	**Chr number estimate**	**Chr total length (Mb)**
	1	2.93	669.83
	2	3.05	736.97
	3	2.75	538.69
	4	2.56	483.53
	5	3.07	546.90
	6	2.61	441.24
	7	2.69	425.22
	8	3.21	465.58
	9	2.88	354.05
	10	3.24	433.80
	11	2.98	395.74
	12	2.61	344.28
	13	2.13	206.20
	14	2.77	246.57
	15	2.72	225.35
	16	2.83	229.01
	17	3.09	247.32
	18	2.66	204.90
	19	2.49	144.16
	20	2.98	181.59
	21	2.69	96.84
	22	4.30	154.68
	X	1.55	233.84
	TOTAL	**64.75**	**8006.27**

Table S3. Heatmap of changes in chromosome copy number (ΔCN), single nucleotide variations (SNV), changes in loss of heterozygosity (ΔLOH) and mRNA ratio from SNPa, aCGH* and RNA-Seq experiments, against data of control clone 1 sample in fig. 5B.

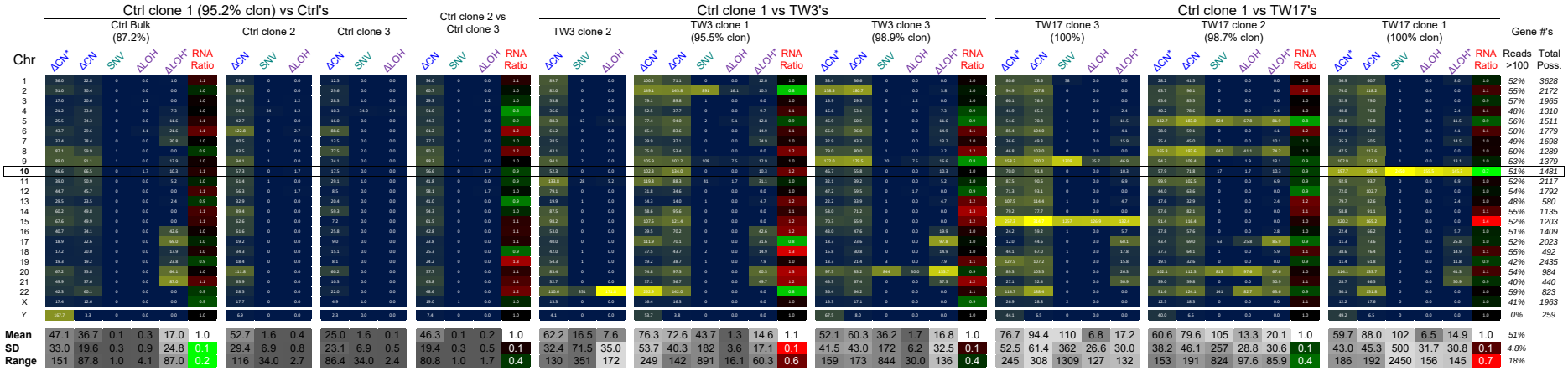

*Data from Agilent's aCGH+SNP array

ΔCN Change in Chromosome Copy number in Mb

SNV Single Nucleotide Variation count

ΔLOH Change in Loss of Heterozygosity in Mb

RNA Ratio Fold change in mRNA level

Table S4. Counts taken from the chromosome copy number change against log_2(RNA ratio) plots shown in Figure 5G. **Only the data points above the 0.5 threshold**, for both changes, were taken into consideration. Relative percentage population of each sample for each quadrants of table S2A. For overall positive correlation, we combined the data as cluster 2 & 3 (C2, C4) versus cluster 1 & 4 (C1, C4), and calculated $p = 3.15 \times 10^{-9}$. Probability of the positive correlation between the chromosome copy number change against log_2(RNA ratio), per counts. Probability of each cluster was cacluated by 0.5^(Count) for the counts listed in upper table. The positive correlation p-value was calculated by (pC3/pC1)*(pC2/pC4).Cluster 1, 2, 3 and 4 represent top left, top right, bottom left and bottom right quadrants of the plot.

Counts	Ctrl Clone 1	Ctrl Clone3	TW3 Clone1	TW3 Clone3	TW17 Clone1	TW17 Clone2
Cluster1	26	20	71	64	60	101
Cluster2	161	178	347	203	384	340
Cluster3	108	164	302	294	246	220
Cluster4	133	135	131	87	226	94
TOTAL	428	497	851	648	916	755
Percentage population						
Cluster1	6.1%	4.0%	8.3%	9.9%	6.6%	13.4%
Cluster2	37.6%	35.8%	40.8%	31.3%	41.9%	45.0%
Cluster3	25.2%	33.0%	35.5%	45.4%	26.9%	29.1%
Cluster4	31.1%	27.2%	15.4%	13.4%	24.7%	12.5%
Probability						
pCluster1	1.5E-08	9.5E-07	4.2E-22	5.4E-20	8.7E-19	3.9E-31
pCluster2	3.4E-49	2.6E-54	3.5E-105	7.8E-62	2.5E-116	4.5E-103
pCluster3	3.1E-33	4.3E-50	1.2E-91	3.1E-89	8.8E-75	5.9E-67
pCluster4	9.2E-41	2.3E-41	3.7E-40	6.5E-27	9.3E-69	5.0E-29
Positive correlation p-value	7.7E-34	5.1E-57	2.8E-135	7.0E-105	2.8E-104	1.3E-110

Table S5. Counts taken from the chromosome copy number change against log_2(RNA ratio) plots shown in Figure 5G. **All data points were taken into consideration.**. Relative percentage population of each sample for each quadrants of table S2A. For overall positive correlation, we combined the data as cluster 2 & 3 (C2, C4) versus cluster 1 & 4 (C1, C4), and calculated p= 0.008. Probability of the positive correlation between the chromosome copy number change against log_2(RNA ratio), per counts. Probability of each cluster was cacluated by 0.5^(Count) for the counts listed in upper table. The positive correlation p-value was calculated by (pC3/pC1)*(pC2/ pC4).Cluster 1, 2, 3 and 4 represent top left, top right, bottom left and bottom right quadrants of the plot.

Counts	Ctrl Clone 1	Ctrl Clone3	TW3 Clone1	TW3 Clone3	TW17 Clone1	TW17 Clone2
Cluster1	96	125	174	275	162	388
Cluster2	818	522	1007	684	863	873
Cluster3	311	735	503	700	410	493
Cluster4	1149	992	690	715	939	620
TOTAL	2374	2374	2374	2374	2374	2374
Percentage population						
Cluster1	4.0%	5.3%	7.3%	11.6%	6.8%	16.3%
Cluster2	34.5%	22.0%	42.4%	28.8%	36.4%	36.8%
Cluster3	13.1%	31.0%	21.2%	29.5%	17.3%	20.8%
Cluster4	48.4%	41.8%	29.1%	30.1%	39.6%	26.1%
Probability						
pCluster1	1.3E-29	2.4E-38	4.2E-53	1.6E-83	1.7E-49	1.6E-117
pCluster2	5.7E-247	7.3E-158	7.3E-304	1.2E-206	1.6E-260	1.6E-263
pCluster3	2.4E-94	5.5E-222	3.8E-152	1.9E-211	3.8E-124	3.9E-149
pCluster4	9.3E-302	2.4E-299	1.9E-208	5.8E-216	2.2E-283	2.3E-187
Positive correlation p-value	1.2E-10	7.2E-43	3.4E-195	2.5E-119	1.7E-52	1.7E-108

Table S6. Results from array-CGH (Comparative Genome Hybridization) for control clone 1 of Figure 4C.

Cell Line GENETICS
www.clgenetics.com
510 Charmany Drive • #254–255 • Madison, Wisconsin 53719 • 608-441-8160

CLG Microarray Test Results

Cell Line ID: U2OS/Control-Clone1 p8 **Lab #:** CLG-21818 **Date received:** 11/6/15 **Date Reported:**11/20/15

Contact Person: Jerome Irianto **PI:** D. Discher **Institute:** University of Pennsylvania

Test Code: aCGH 150 **Email:** iriantoj@seas.upenn.edu **PO #:** 3473145

Mailing Address: 129 Towne Building, 220 S. 33rd St., Philadelphia, PA 19104

Sample Type: Human Epithelial Frozen Culture **dsDNA Concentration:** 218ng/µl **Total dsDNA:** 3.2 µg

Sex: Female **260/280** (1.7-1.9): 1.8 **260/230** (≥1.90): 2.2 **Array Type:** Agilent 180K Standard aCGH +SNP

Array ID Number: 252983030028_1_1 **Reference DNA:** Agilent Euro Female

---

Quality Control
A sufficient amount of high quality genomic DNA, as determined by UV spec. (NanoVue), fluorometer (Qubit) and Agarose Gel analysis, was extracted from cell line U2OS/Control-Clone1 p8 and passed our internal quality standards for aCGH labeling.

aCGH Probes (PASS/FAIL): Pass
SNP Probes (PASS/FAIL): Pass

Experimental Deviations: None

Results:
Clonal Fraction: 95.17%

See attached sheets for Tabular and Graphical presentation of microarray results.

Variants are considered provisional until confirmed by another technique. For further confirmation of a particular variant, CLG recommends using Karyotyping (variants >5Mb), FISH (variants>200Kb).

Supplemental References

S1. Irianto, J., Pfeifer, C.R., Bennett, R.R., Xia, Y., Ivanovska, I.L., Liu, A.J., Greenberg, R.A., and Discher, D.E. (2016). Nuclear constriction segregates mobile nuclear proteins away from chromatin. Mol. Biol. Cell. DOI: 10.1091/mbc.E16-06-0428

S2. Talevich, E., Shain, A.H., Botton, T., and Bastian, B.C. (2016). CNVkit: Genome-Wide Copy Number Detection and Visualization from Targeted DNA Sequencing. PLoS Comput. Biol. 12, e1004873.